

Discovery of 26 new Galactic radio transients by MeerTRAP

J. D. Turner,^{1*} B. W. Stappers,¹ J. Tian,¹ M. C. Bezuidenhout,^{2,3} M. Caleb,⁴ L. N. Driessen,⁴ F. Jankowski,⁵ I. Pastor-Marazuela,¹ K. M. Rajwade,⁶ M. Surnis,⁷ M. Kramer,^{8,1} E. D. Barr,⁸ M. Berezina,^{8,9}

¹ Jodrell Bank Centre for Astrophysics, Department of Physics and Astronomy, The University of Manchester, Manchester M13 9PL, UK

² Department of Mathematical Sciences, University of South Africa, Cnr Christiaan de Wet Rd and Pioneer Avenue, Florida Park, 1709, Roodepoort, South Africa

³ Centre for Space Research, Potchefstroom Campus, North-West University, Potchefstroom 2520, South Africa

⁴ Sydney Institute for Astronomy, School of Physics, The University of Sydney, New South Wales 2006, Australia

⁵ LPC2E, OSUC, Univ Orleans, CNRS, CNES, Observatoire de Paris, F-45071 Orleans, France

⁶ Astrophysics, The University of Oxford, Denys Wilkinson Building, Keble Road, Oxford OX1 3RH, UK

⁷ Department of Physics, IISER Bhopal, Bhauri Bypass Road, Bhopal, 462066, India

⁸ Max-Planck-Institut für Radioastronomie, Auf dem Hügel 69, D-53121 Bonn, Germany

⁹ Landessternwarte, Universität Heidelberg, Königstuhl 12, D-69117 Heidelberg, Germany

Accepted XXX. Received YYY; in original form ZZZ

ABSTRACT

Radio searches for single pulses provide the opportunity to discover one-off events, fast transients and some pulsars that might otherwise be missed by conventional periodicity searches. The MeerTRAP real-time search pipeline operates commensally to observations with the MeerKAT telescope. Here, we report on 26 new Galactic radio transients, mostly rotating radio transients (RRATs) and also the detection of one RRAT and two pulsars that were independently discovered by other surveys. The dispersion measures of two of the new sources marginally exceed the Galactic contribution depending on the electron density model used. Using a simple method of fitting a Gaussian function to individual pulses, and obtaining positions of arcsecond accuracy from image-based localisations using channelised voltage data from our transient buffer, we have derived timing solutions spanning multiple years for five sources. The timing parameters imply ages of several Myr and low surface magnetic field strengths which is characteristic of RRATs. We were able to measure spin periods for eight more transients, including one source which appears to rotate every 17.5 seconds. A majority of the sources have only been seen in one observation, sometimes despite multiple return visits to the field. Some sources exhibit complex emission features like component switching and periodic microstructure.

Key words: stars: neutron – pulsars: general – radio continuum: transients

1 INTRODUCTION

Radio-emitting neutron stars (NSs) are known as pulsars if they appear to flash or pulse as their magnetic axis sweeps across the line of sight to an observer. Most pulsars have been discovered using Fourier-domain periodicity searches. However, these searches disfavour the discovery of intermittent sources like Rotating Radio Transients (RRATs;¹ Keane & McLaughlin 2011), as they do not have significant spectral power. Currently, 155 out of the 211 RRATs in the ATNF Pulsar catalogue² (Manchester et al. 2005) have a period measurement, and 44 of those also have a period derivative. After their discovery (McLaughlin et al. 2006), efforts to reprocess survey data to find single dispersed pulses (e.g. Keane et al. 2010; Michilli et al. 2018) led to the discovery of many new RRATs. As a result, it has become the standard practice to include a single pulse search pipeline parallel to pulsar searches. Multibeam receivers provide a

larger field-of-view (FoV) which boosts the chances for discoveries during those searches (Burke-Spolaor & Bailes 2010; Burke-Spolaor et al. 2011; Keane et al. 2018; Karako-Argaman et al. 2015; Deneva et al. 2016; Patel et al. 2018; Tyul’bashev et al. 2018; Zhou et al. 2023). Interferometric real-time searches can potentially access a larger FoV, offer more sensitivity and provide instantaneous localisations, e.g. the Canadian Hydrogen Intensity Mapping Experiment (CHIME; CHIME/FRB Collaboration et al. 2018) and the Commensal Realtime ASKAP Fast Transient COherent searches (CRACO; Wang et al. 2024). The continued discovery and timing of RRATs by these surveys provides an improved opportunity to constrain their emission states (e.g. Zhou et al. 2023), constrain the Galactic NS birth rate (Keane & Kramer 2008) and inform how future transient searching surveys should operate.

Aside from RRATs, these surveys are sensitive to very long period pulsars that lie beyond the pulsar death line. The 76-second pulsar discovered by Caleb et al. (2022a) is so far from canonical pulsars in rotational phase-space that it could belong to the hypothesised ultra-long period magnetar class of NS (Beniamini et al. 2023). The 421-second transient discovered by CHIME (Dong et al. 2024) is a member of the long-period transient (LPT) class of very slow rotators, potentially NSs, capable of producing beamed coherent radio emission. At the

* E-mail: james.turner-13@postgrad.manchester.ac.uk

¹ RRATs are generally treated as a separate class from nulling pulsars: RRATs tend to be more transient and are characterised by a dramatic variability in brightness, while nullers tend to spend time between a bright and non-visible state.

² <https://www.atnf.csiro.au/research/pulsar/psrcat/> v2.2.0

same time, fast image-domain searches have discovered even slower LPTs, for example the 18-minute GLEAM-X J162759.5–523504.3 (Hurley-Walker et al. 2022b), the 21-minute GPMJ1839–10 (Hurley-Walker et al. 2023) and the 54-minute ASKAP J193505.1+214841.0 (Caleb et al. 2024). The slowest pulsars and LPTs pose challenges to our understanding of radio emission from a slowly rotating dipole and provide clues as to how NSs are born and evolve.

The MeerKAT telescope (Jonas 2018; Camilo et al. 2018) in South Africa is the most sensitive telescope in the Southern hemisphere. MeerTRAP (more TRAnsients and Pulsars with MeerKAT, for project details see Sanidas et al. 2018) has since September 2020 been searching for fast radio transients in real-time by piggybacking on a significant portion of MeerKAT observations. This has resulted in the discovery of 14 Galactic transients (Caleb et al. 2022a; Bezuidenhout et al. 2022; Surnis et al. 2023), excluding those presented here, and a few dozen fast radio bursts (FRBs). FRBs are short duration, extra-galactic radio pulses of unknown physical origin (see Cordes & Chatterjee 2019; Petroff et al. 2022, for a review). Due to the large data volumes of ≈ 21 GB/s handled by the MeerTRAP transient search backend, data must be irreversibly reduced in frequency or time resolution to be searched. The role of the transient buffer, which has been in operation since June 2022, is to retain a full, or near-full resolution copy of the data to be deposited on demand for offline analysis. This has proven essential in rapidly localising and following-up MeerTRAP discoveries, including FRBs (Rajwade et al. 2024). Section 2 briefly describes the key components of the real-time search pipeline and the transient buffer, and details the offline processing of the data. In Section 3 we present the newly discovered sources and their properties. In Section 4 we interpret the discoveries and the method for calculating pulse arrival times and in Section 5 we summarise our findings and conclude.

New sources are given the MeerTRAP name ‘MTPXXXX’, which is based on the chronology of discoveries. A standard J2000 name is also given for sources where we have measured a spin period. We report all detections of these sources up to 2024 July 25. Throughout the article, bracketed values that follow results refer to the 1-sigma uncertainty on the final digit. All timestamps provided are topocentric and are dispersion-corrected to the highest frequency of the observing band, unless stated otherwise.

2 OBSERVATIONS AND DATA REDUCTION

2.1 MeerKAT data processing

Real-time pulse searches

MeerTRAP piggybacks many MeerKAT observations, of which a significant fraction have been during time dedicated to Large Survey Projects (LSPs). LSPs tend to focus on a particular class of sources or region of the sky. Consequently, MeerTRAP does not uniformly sample the Southern sky, as some fields are frequented often and others rarely or not at all (see Bezuidenhout et al. 2022). MeerTRAP’s frequency coverage depends on the MeerKAT receiver in use. These data here were captured by the L-band receiver (856–1712 MHz; Lehmsiek & Theron 2012) or the Ultra High Frequency (UHF)–band receiver (544–1088 MHz; Lehmsiek & Theron 2014). Two observing modes are operated simultaneously; in the incoherent mode the signals from the receivers of up to 64 telescopes are combined to form the incoherent beam (IB), and in the coherent mode the signals are coherently summed with respect to the phase centre of the array. Up to 768 coherent beams (CBs) are instantaneously formed on the sky as computed by the Filterbanking Beamformer

User Supplied Equipment (FBFUSE; Barr 2018; Chen et al. 2021) a dedicated high-performance cluster installed on-site. Usually, the innermost 40 telescopes with a 1 km baseline are used instead of the full array to balance sky coverage and system gain. The central CB is therefore a factor of around $40/\sqrt{64} \approx 5$ times more sensitive than the IB (e.g., Rajwade et al. 2022). To ensure the sensitivity of the coherent FoV exceeds that of the IB, the beam overlap is chosen to be at 25 per cent of the peak sensitivity level.

Channelised data from FBFUSE are transferred to the Transient User Supplied Equipment (TUSE) cluster then downsampled and processed by the real-time search pipeline. The specifications of the data are provided in Table 1. The IB area³ is computed by Jankowski et al. (2023) at the half-power width, and the CB widths refer to the width at the overlap level. The typical smallest half-power width of a CB is ~ 80 arcsec at 816 MHz and ~ 50 arcsec at 1284 MHz. The CB shape strongly depends on the available baselines and the source elevation, so Table 1 provides the central 90 per cent range of widths. The MeerTRAP search pipeline was introduced in Malenta et al. (2020) and later described in detail in Rajwade et al. (2021, 2022) and Bezuidenhout et al. (2022). Table 1 lists the search parameters and excision thresholds applied to the candidates. Radio frequency interference (RFI) is mitigated with the zero-DM technique (Eatough et al. 2009; Men et al. 2019) and with IQRM⁴ (Morello et al. 2022). Broadband RFI is further mitigated by rejecting candidates below a dispersion measure (DM) of 20 pc cm^{-3} . The maximum DM trials were previously 1480 pc cm^{-3} (UHF) and 5000 pc cm^{-3} (L-band), but were set to 2100 pc cm^{-3} and 3600 pc cm^{-3} respectively in October 2023. Candidates above the signal-to-noise ratio (S/N) threshold are then sifted and classified (see Rajwade et al. 2022, for further information) using FRBID⁵ (Hosenie 2021). Initially, the S/N threshold was varied between 7–8 depending on RFI prevalence, but has been set at 8 since October 2021. Candidates are written as a filterbank in SIGPROC⁶ format and padded with 0.5 s of data either side of the pulse. For any candidate of $S/N < 8$, the data are checked using the MeerTRAP candidate inspection tool MTCUTILS⁷ to see if the DM can be optimised to extract enough S/N to claim a detection. During observations, a JSON file is written to TUSE that contains information about the user’s observation, such as the target, the telescopes and the beam positions. These are created every 10 minutes or every new target, whichever is sooner.

Localisation

We seek to rapidly localise our new discoveries so that when the field is reobserved, we can strategically form a coherent beam at the best position to achieve a better sensitivity and detect more pulses. We refer to this setup as a targeted observation. A detection in a single CB indicates the pulse originated within that region, provided the beam does not lie on the edge of the tiling. If a pulse is detected in three or more CBs, we can use spatial S/N variation to constrain the position, usually to within a few arcseconds. To do this, we use the multibeam localisation tool SEEKAT⁸ (Bezuidenhout et al. 2023). We provide SEEKAT with a coherent point spread function (PSF)

³ In some previous MeerTRAP papers the FoV was given as 1.27 deg^2 which was calculated assuming a central frequency of about 1120 MHz.

⁴ <https://github.com/v-morello/iqrm>

⁵ <https://github.com/Zafirah13/FRBID> by Zafirah Hosenie

⁶ <https://sigproc.sourceforge.net/>

⁷ <https://bitbucket.org/vmorello/mtcutils> by Vincent Morello

⁸ <https://github.com/BezuidenhoutMC/SeeKAT> by Mechiel Bezuidenhout

Table 1. Specification summary of MeerTRAP data and the search pipeline. Beam widths are given at the central frequency of the observing band. These values are true for the majority of searches; details of how the thresholds have been varied are given in the text. The CB widths are the beam widths at the 0.25 level overlap.

Data specifications		
	UHF	L-band
Central frequency, MHz	816	1284
Bandwidth, MHz	544	856
Sampling time, μ s	482	306
Number of channels		1024
Number of polarisations		2
CB overlap level		0.25
90% CB width range, arcsec	76-228	46-100
Half-power IB area, deg ²	2.4	1.0
Pipeline thresholds		
Min. DM, pc cm ⁻³		20
Max. DM, pc cm ⁻³	1480-2100	3600-5000
Min. boxcar width, s	0.000482	0.000306
Max. boxcar width, s	0.25	0.67
S/N cutoff		7-8
IQRM maximum lag, samples		100
IQRM threshold, σ		3.0

simulated by the multibeam simulation package `MOSAIC`⁹ described in [Chen et al. \(2021\)](#).

We can also use voltage data captured by the transient buffer (TB) ([Malenta et al. 2020](#); [Jankowski et al. 2022](#)), in operation since June 2022. Several of the new source triggered the TB, allowing image-based localisations. A detailed description of the TB and the formation of measurement sets (MSs) from the voltage data using `CASA` ([McMullin et al. 2007](#)) is given in [Rajwade et al. \(2024\)](#). The system does not distinguish FRBs from other transients, thus we follow the same data reduction process described in [Rajwade et al. \(2024\)](#) and [Tian et al. \(2024\)](#). Usually, data from ~ 60 telescopes is saved, thus providing more sensitivity than the CB or IB detections in the time domain. Subbanded MSs are cleaned with `WSClean` ([Offringa et al. 2014](#)) then frequency-averaged ‘on-’ and ‘off-pulse’ images, separated by a few dozen milliseconds, are compared. Once identified, the best position and uncertainty of the emission is found using `PYTHON` Blob Detector and Source Finder, `pyBDSF`¹⁰. The position is corrected by performing absolute astrometry using catalogued sources in the field with position of sub-arcsecond accuracy. These measurements follow the same methodology as is described in [Driessen et al. \(2022, 2024\)](#). All matched sources used to solve for a transformation matrix to shift and rotate the MeerKAT sources were Rapid ASKAP Continuum Survey (RACS) source positions¹¹. The total uncertainty is typically about 1 arcsec, and has three contributions: the uncertainty from the fit in `PYBDSF`, the absolute systematic astrometric uncertainty from the RACS positions ([Hale et al. 2021](#); [Duchesne et al. 2024](#)) and the median offset of the positions after the astrometric correction.

⁹ <https://github.com/wchenastro/Mosaic> by Weiwei Chen

¹⁰ <https://www.astron.nl/citt/pybdsf/>

¹¹ The code for performing the astrometric correction can be found on GitHub: https://github.com/AstroLaura/MeerKAT_Source_Matching

2.2 Determining the dispersion measure

For each source we report either the DM that optimises the S/N of the pulse or the DM that optimises for frequency-averaged profile structure. For all sources, we measure the DM of the brightest pulse and assume it is the correct DM for all other pulses. Structure-optimised dispersion correction is preferred over optimising S/N for pulses with complex profiles and frequency-time substructure ([Hessels et al. 2019](#)). As has been the case for many one-off and repeating FRBs (e.g. [Sand et al. 2024](#)), this method can help reveal underlying substructure in our source, so we used this method for as many sources as possible. To measure the structure-optimised DM we use `DM_PHASE`¹² ([Seymour et al. 2019](#)). `DM_PHASE` does not clean the data of RFI, so we do this before hand using `IQRM_APOLLO`¹³ ([Morello et al. 2023](#); also see [Morello et al. 2022](#) for more details). If `DM_PHASE` is not suitable due to low S/N or only single component pulses are seen, we use `SCATFIT`¹⁴ ([Jankowski 2022](#)), which models subbanded pulse profiles as an exponentially-modified Gaussian pulse that is broadened due to the dispersive and scattering action of the interstellar medium and smearing due to intra-channel dispersion and the time resolution. `SCATFIT` uses a Bayesian analysis by Markov Chain Monte Carlo sampling to provide a refined DM and uncertainty. More details can be found in [Jankowski et al. \(2023\)](#). Using the brightest single-component pulse for each source, we fit a scattered pulse model. Due to the low S/N of many of these pulses, we trial the fit for data that are downsampled in time by a factor of 2 and 4, and in frequency to 4, 8 and 16 subbands, and choose the DM with the best Bayesian information criterion (BIC) and reduced- χ^2 closest to unity. Subbands with a S/N value below 3.0 are not included in the fit. If a scattering timescale cannot be measured across all subbands, we instead fit an unscattered model. We did this instead of allowing the scattering timescale to fall to zero to avoid it correlating with the smearing timescale.¹⁵ We ultimately did not find a scattered profile to be better than the unscattered model for any of the pulses. The results from the fits are provided in [Table A1](#).

2.3 Properties and timing of single pulses

For some sources we detected a cluster of pulses in a single day from which we could use their separation in time to measure the spin period, P . Of these sources, there were some with detections spanning many days from which we could measure the spin-down rate, \dot{P} and constrain the position using pulsar timing. In order to do this we calculated the time of arrival (TOA) of the signal for each detection. We must do this to each pulse individually, as only a portion of the rotation phase is contained in the data stored for each detection. The TOAs are calculated using `make_toas`¹⁶, an implementation of `MTCUTILS`. For each pulse (the brightest if there are multibeam detections), `make_toas` finds the width and phase alignment that

¹² https://github.com/InesPM/DM_phase by Andrew Seymour, Daniele Michilli and Ziggy Pleunis, modified by Inés Pastor-Marazuela

¹³ https://gitlab.com/kmrajwade/iqrm_apollo

¹⁴ <https://github.com/fjankowsk/scatfit> by Fabian Jankowski

¹⁵ `SCATFIT` contains models that consider DM smearing between channels, though we can ignore this as the smearing timescale is less than the intrinsic pulse width at the bottom of the band for all the pulses we inspected.

¹⁶ Available at: <https://bitbucket.org/meertrap-ipm/mtcutils/src/jturner-timing/>

maximises the S/N by using `SPYDEN`¹⁷ to convolve single-Gaussian templates of various widths with the time series. This is done on the full time resolution data dedispersed at the best DM to the top of the frequency band. The dispersion delay-corrected timestamp of the first bin is added to the time of the peak bin of the best Gaussian to get the TOA. The uncertainty on the TOA is calculated to be the width of the pulse divided by the S/N. With this method, the uncertainty due to pulse jitter is worse than conventional pulsar timing, because we fit to the feature in intensity that best resembles a Gaussian. Additionally, we may inadvertently fit to substructure or subpulses that would not otherwise be a dominant pulse component. However, the width of any subpulse is always smaller than the full pulse width, so our TOA value will not be greatly affected by this.

To make an initial period estimate of some pulses that are closely spaced in time, we use `RRATSOLVE`¹⁸ to find the lowest common period connecting the TOAs. The period returned is the largest value that connects the TOAs, such that P/N where N is an integer is also a valid solution. If we have pulses over multiple days, we use the pulsar timing program `TEMPO2`¹⁹ (Hobbs et al. 2006) to find a phase-connected timing solution. Our initial timing model is an ephemeris containing the period from `RRATSOLVE` and a position obtained either from `SEEKAT` or from imaging. Then using `TEMPO2`, we find the barycentric rotational parameters and, if possible, a constrained position that best predicts the TOAs. The rapid and accurate localisations improve our ability to obtain a timing solutions even with a low number of TOAs.

The timestamps recorded in the JSONs from TUSE are used to calculate the total observation time and analyse the detection statistics of the new sources. Specifically, we use the total time spent observing any targets during which a new source was detected; we henceforth refer to these as primary targets (e.g. the primary target for observations of the new source MTP0014 is the gain calibrator J1911–2006). For the case where detections are, or would be, serendipitous we define a non-targeted observing time, T_n . For targeted observations (see Section 2.1 ‘Localisation’), we separately calculate a targeted observing time, T_t . We make calculations of the average detection rate for several sources using T_n or, where possible, T_t . Due to how the MeerTRAP system operates, the real-time search does not include approximately 25 s of data per new pointing. The amount of unsearched data varies, so we provide an uncertainty on T_n and T_t that assumes the 25 s time loss has an error of 50 per cent. The fractional uncertainty is thus lower where integration times are longer.

T_n must be considered a lower limit as there may be observations of other sources in the field of our discoveries where detections were not made. We assume in such cases that if there are no detections, then either the observing time was not significant or the source was not covered by CBs. With this caveat in mind, we make two statements about our calculations. Firstly, the average non-targeted detection rate must be considered an upper limit if T_n is a lower limit. Secondly, the targeted detection rate is much more reliable, given the unchanging beam position and the extra sensitivity. Although the full sensitivity provided by MeerKAT’s coherent observing mode allows us to sample fainter pulses, the rates we find are ultimately flux-limited. Detailed analyses of pulse energy distributions are beyond the scope of this paper. The pulse statistics will also be biased by the nature of the primary targets. For example, if a source is in the field of

a calibrator, then those observations will tend to sample short wait times between pulses.

3 RESULTS

3.1 Sources published elsewhere

We provide here information about three sources that were new at the time of detection, but were concurrently seen in other surveys. The properties of the detections and pulses are given in Table 2. The discovery S/N is that of the first pulse as seen by the real-time MeerTRAP pipeline. The definitions of the targeted and non-targeted detection rates are described in Section 2.3. The position, DM, S/N determined by `SPYDEN` and spin period values are provided in Table 3. DM-derived distances from the NE2001 (Cordes & Lazio 2002) and YMW16 (Yao et al. 2016) Galactic electron density models are obtained using the `pygedm`²⁰ tool (Price et al. 2021).

MTP0015/PSR J2237+2828 was discovered by MeerTRAP on MJD 59177 in a CB. The pulse profile and the dynamic spectrum are shown in the leftmost plot of Figure 1. It was also detected by the CHIME telescope on MJD 59193 by Dong et al. (2023). They found a spin period of 1.077 s and DM of 38.1 pc cm^{-3} . PSR J2237+2828 is located only 14’ from the L-band gain calibrator²¹ J2236+2828. Since our first detection, two more pulses have been seen in approximately 98 minutes of targeted observing time, giving a targeted detection rate of 1.2 hr^{-1} , which is below the rate reported across CHIME observations in Dong et al. (2023). If we include the discovery pulse, albeit non-targeted, this gives a rate of 1.8 hr^{-1} which is more closely aligned to the value from CHIME observations. Regardless, both are consistent if a Poissonian pulse rate and uncertainty are assumed. Interestingly, we have not detected a population of fainter pulses when targeting PSR J2237+2828, only very bright pulses of $S/N > 50$. The source scintillates across the band and has some microstructure within a main peak. The brightness of the pulses and microstructure allowed us to find a structurally-optimised DM using `DM_PHASE` of $38.1 \pm 0.1 \text{ pc cm}^{-3}$, which matches the DM measured by Dong et al. (2023).

MeerTRAP commensally observed with the L-band portion of the Max-Planck-Institut für Radioastronomie (MPIfR)–MeerKAT Galactic Plane Survey (MMGPS–L; Padmanabh et al. 2023). Two of the pulsars discovered up to that point by the survey²² have single pulses bright enough to be detected by the MeerTRAP pipeline. These are MTP0028/PSR J1540–5821 and MTP0043/PSR J1649–4230 and we provide here some information about their properties supplementary to those given by Padmanabh et al. (2023). Of all the 78 pulsars discovered by MMGPS–L, PSR J1540–5821 has the longest period, 3.47472(7) s and a DM of $427 \pm 3 \text{ pc cm}^{-3}$. MeerTRAP detected three pulses in the same CB at much higher DMs between 439–441 pc cm^{-3} . We checked the data in `mtcutils/candreport` and visual inspection of a range of DMs showed that MMGPS–L DM value is too low to fully dedisperse the pulse. With `SCATFIT` we obtained a refined DM value of $440.3 \pm 0.2 \text{ pc cm}^{-3}$, which dedisperses the data to produce the dynamic spectrum in Figure 1, and is consistent to 5-sigma with the MMGPS–L value. The S/N range of the MeerTRAP pulses is 5–11 when dedispersed at the 427 pc cm^{-3} and 13–23 at 440.3 pc cm^{-3} .

¹⁷ <https://bitbucket.org/vmorello/spyden> by Vincent Morello

¹⁸ <https://github.com/v-morello/rratsolve> by Vincent Morello

¹⁹ <https://bitbucket.org/psrsoft/tempo2/src/master/>

²⁰ <https://github.com/FRBs/pygedm>

²¹ A list of calibrator sources that are recommended for users of MeerKAT is provided here by SARAO.

²² MMGPS discoveries are listed at trapum.org/discoveries.

Table 2. Detection and observation information for all of the reported transients, starting with their names and the date, observing mode and candidate S/N of their discovery pulses. Two detection counts are provided; the non-targeted number, $N_{\text{det},n}$ is the count during the time T_n spent observing any identified nearby primary target(s) at L-band and UHF combined, and $N_{\text{det},t}$ is for the time, T_t when the source was targeted. The total number of non-targeted and targeted observations, N_{obs} is given, and the frequency band at which detections have been made. The typical length of observations is approximately T/N_{obs} , but more detail is provided in the text for each source.

MTP name	PSR J2000 name	Discov. MJD	Discov. mode	Discov. S/N	$N_{\text{det},n}$	T_n (s)	$N_{\text{det},t}$	T_t (s)	N_{obs}	Band
Published sources										
MTP0015	J2237+2828	59177.713493	CB	37.8	1	271(13)	2	6009(124)	99	L
MTP0028	J1540–5821	59436.852030	CB	10.1	3	572(13)	–	0	1	L
MTP0043	J1649–4230	59579.482282	CB	10.0	2	553(13)	–	0	1	L
New sources										
MTP0014	J1911–2020	59177.610266	CB	9.8	10	1210(47)	650	31834(267)	471	L, UHF
MTP0016		59208.082669	CB	8.4	4	4100(50)	–	0	16	L
MTP0017	J0402–6542	59214.773203	CB	9.4	2	63846(178)	133	345590(446)	1446	UHF
MTP0018		59215.933480	IB	8.5	1	410414(790)	–	0	1446	UHF
MTP0020	J1930–1856	59324.147363	CB	8.5	16	40648(108)	235	34290(101)	26	L, UHF
MTP0021	J0219–06	59330.512419	IB, CB	7.0	6	22175(106)	–	0	13	L
MTP0022		59344.674851	CB	9.2	4	2860(44)	0	2942(69)	6	L
MTP0023	J1319–4536	59369.833079	IB, CB	18.2	39	42982(272)	52	7284(100)	799	L, UHF
MTP0024		59372.073761	IB	9.9	2	21254(38)	–	0	6	L
MTP0026		59390.962435	CB	7.9	1	565(28)	–	0	1	L
MTP0029		59446.907329	CB	13.9	3	560(13)	–	0	1	L
MTP0031	J0917–4245	59448.261286	IB, CB	22.9	30	9064(67)	–	0	25	L, UHF
MTP0032		59499.647428	CB	7.9	1	569(13)	–	0	1	L
MTP0034	J1108–5946	59513.466697	IB, CB	8.5	135	3095(40)	–	0	4	L
MTP0035	J1308–61	59513.543102	IB	12.3	2	574(13)	–	0	1	L
MTP0036		59517.055729	CB	8.9	1	201(18)	–	0	1	L
MTP0038		59557.258616	CB	16.7	1	56973(149)	–	0	17	L
MTP0039	J1533–5609	59559.185447	CB	8.5	71	54032(137)	0	1291(53)	33	L
MTP0040		59564.389209	CB	9.3	1	548(13)	0	94(13)	2	L
MTP0042	J1641–5109	59495.789294	CB	10.0	2	545(13)	–	0	1	L
MTP0044		59581.544680	CB	15.5	9	6586(44)	–	0	6	UHF
MTP0045		59568.125229	CB	8.8	28	83633(185)	1	3808(71)	39	L
MTP0046		59594.430739	CB	9.0	1	535(13)	–	0	1	L
MTP0047		59595.470964	CB	8.3	2	181(18)	6	1041(45)	12	L
MTP0048		59613.248703	CB	9.2	2	557(13)	–	0	1	L
MTP0049		59616.254504	CB	10.0	1	1013(18)	–	0	2	L

We do not have a robust explanation as to why the MMGPS–L DM is so low, though we note there is some RFI still present in the diagnostics plots that may have affected their measurement. We measured TOAs for the three pulses and found they are fully consistent with the separation predicted by the period reported by Padmanabh et al. (2023).

PSR J1649–4230 was detected in MMGPS–L at a period of 0.676 s and a DM of 374 ± 6 pc cm^{−3}. Two faint pulses from PSR J1649–4230, the first of which is shown in Figure 1 were concurrently detected by MeerTRAP. The TOAs we measured are consistent with their period to 4-sigma. They are at least 60 ms in width and exhibit a tenuously visible precursor component to the main peak. We relay the best DM reported by Padmanabh et al. (2023) of 374 ± 6 pc cm^{−3} as our methods did not provide an improved measurement. Due to how TUSE pads the candidate data, a further three spin period lengths were kept. We inspected the DM-time planes at integer periods after both pulses and saw very faint signals where the next pulses should be. Using the MMGPS–L DM we dedispersed individual windows of data 0.2 s wide around each of the three potential pulses, but did not see anything above a S/N of 7. We therefore claim detections for two pulses only, though it suggests the pulse energy distribution contains some pulses just below our detection threshold.

3.2 New sources

In this section we present the 26 new Galactic transients we have detected. Information about their discovery and observations is shown in Table 2, and their measured properties are listed in Table 3. For five of these sources we were able to find timing solutions, which are given in Table 4. We proceed with detailed descriptions of the sources that have been detected on multiple epochs. The other sources are summarised at the end of this section.

MTP0014/PSR J1911–2020

MTP0014/PSR J1911–2020 was discovered on 2020 November 24 when a cluster of pulses were detected at a DM of ~ 72 pc cm^{−3}. The dynamic spectrum and the frequency-integrated pulse profile is shown for the first of these pulses in the top left of Figure 2. We have since constrained the DM to 71.30 ± 0.03 pc cm^{−3} with SCATFIT using the brightest pulse seen so far, which was on 2023 March 8. A spin period of 4.467 s was initially found using RRATSOLVE on the discovery pulses. PSR J1911–2020 is located very close to the gain calibrator J1911–2006 used by many observers, so of the MeerTRAP sources it has been seen on the most days and has the largest number of detections.

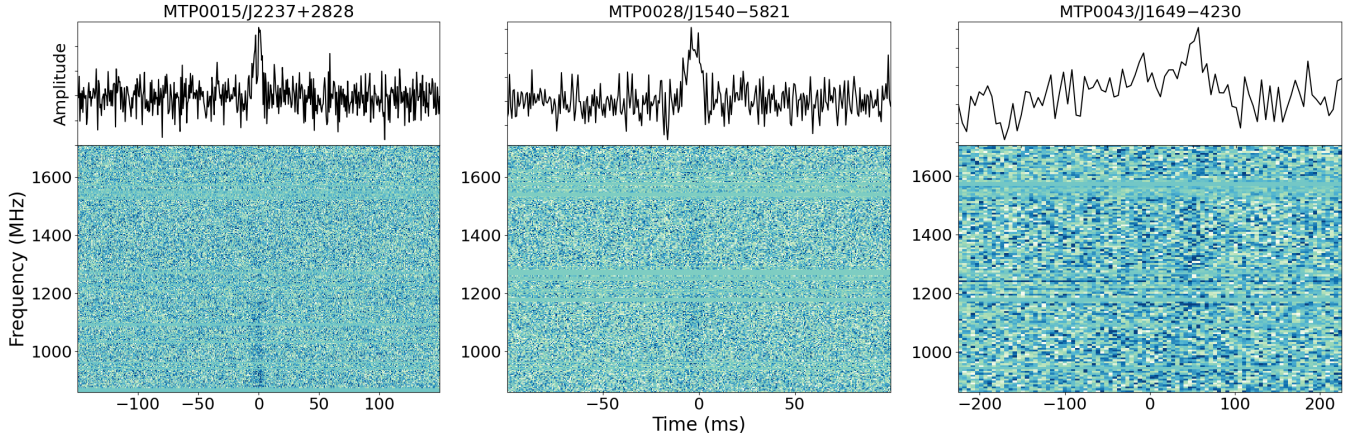


Figure 1. Dynamic spectra (bottom) of the first pulses seen by MeerTRAP for the RRAT PSR J2237+2828 and the two pulsars PSR J1540–5821 and PSR J1649–4230, and their frequency-averaged pulse profiles (top). They have been dedispersed at the best DM which is given in Table 3. The blank horizontal lines are masked channels that were affected by RFI.

Table 3. Properties of the independently discovered pulsars MeerTRAP detected and the new Galactic radio transients. If a position does not have an uncertainty, this is because a proxy for the positional uncertainty is provided in the text, rather than not at all. For all periods we provide the reference epoch for the midpoint of the TOA range used in the calculation. For five sources, the epoch is provided as part of a complete timing solution in Table 4. Upper limits on periods correspond to the minimum time between two pulses. References to publications; [1] Dong et al. (2023) and [2] Padmanabh et al. (2023).

MTP name	RA (J2000) (hh:mm:ss)	Dec (J2000) (dd:mm:ss)	DM (pc cm ⁻³)	Dist. NE2001/YMW16 (kpc)	S/N	Period, P (s)	P Epoch (MJD)
Published sources							
MTP0015	22:37:29.41	+28:28:40	38.1(1) [†]	2.3 / 4	12–160	1.0773950915(3) [1]	–
MTP0028	15:40:10.6	–58:21:56	440.3(2)	8.6 / 11.8	14–23	3.47472(8) [2]	–
MTP0043	16:49:47	–42:30:21	374(6) [2]	5 / 7.1	9–11	0.67641(4) [2]	–
New sources							
MTP0014	19:11:16.05(8)	–20:20:02(9)	71.30(3)	2.1 / 4.2	8–54	4.46792112045(2)	see Table 4
MTP0016	15:25:06.4	–23:22:19	41.2(3)	1.7 / 3.0	13–22	5.5719(2)	59208.083669
MTP0017	04:02:52.25(3)	–65:42:43.46(16)	31.5(2)	1.5 / 2.7	8–19	3.0335229848(1)	see Table 4
MTP0018	04:08:00	–65:45:00	38.8(3)	2.3 / >25	10	–	–
MTP0020	19:30:41.880(92)	–18:56:28.49(12)	63.143(9)	2.1 / 4.3	8–75	1.76083292608(5)	see Table 4
MTP0021	02:19:00	–06:10:00	8.46(7) [†]	0.4 / 0.4	22–132	1.87868(4)	59330.517875
MTP0022	12:43:41.07	–64:23:07.2	342(2) [†]	7.0 / 10.2	14–29	–	–
MTP0023	13:19:48.24(4)	–45:36:04.0(4)	40.41(8) [†]	1.3 / 1.3	8–220	1.8709058201(1)	see Table 4
MTP0024	18:08:27.65	–36:58:43.9	41.0(5)	1.1 / 1.1	12–13	–	–
MTP0026	15:39:40	–61:10:15	206.8(3)	4.5 / 7.4	10	–	–
MTP0029	16:48:36.46	–51:42:46.5	201.4(2)	4.1 / 6.1	10–17	–	–
MTP0031	09:17:28.3(1)	–42:45:55(1)	97.7(3) [†]	0.6 / 0.4	8–68	2.5519(1)	59699.588283
MTP0032	14:52:34.91	–62:35:06.0	271.5(5)	6.1 / 6.1	11	–	–
MTP0034	11:07:58.56(23)	–59:47:01.1(1)	92.7(4)	2.1 / 1.5	8–28	1.516531550(3)	see Table 4
MTP0035	13:08:59	–61:17:00	224.5(2)	4.4 / 5.6	11–12	≤3.9548	59513.543146
MTP0036	10:00:58.60	–51:45:52.9	128.9(7)	3.1 / 0.4	9	–	–
MTP0038	17:27:25.11	–29:42:20.6	126.7(4)	2.4 / 3.0	16	–	–
MTP0039	15:33:50.46	–56:09:29.7	95.31(9)	1.8 / 2.5	8–39	1.06167(1)	59568.370608
MTP0040	13:57:49.48	–65:07:40.7	264(1)	5.6 / 6.4	9	–	–
MTP0042	16:41:39.43	–51:09:00.8	250.4(7)	4.6 / 5.8	13	≤5.5143	59495.789312
MTP0044	22:18:23.3(19)	+29:02:56(33)	55.8(4)	4.4 / >25	8–16	17.49487(3)	59581.575764
MTP0045	15:31:08.0(2)	–55:57:29(2)	56.6(6)	1.3 / 1.2	8–17	2.919875(2)	59568.259968
MTP0046	15:58:46.25	–48:38:48.4	254(1)	8.1 / 6.8	9	–	–
MTP0047	18:07:10.36	–11:51:08.2	152.4(4)	3.4 / 3.5	8–19	–	–
MTP0048	14:29:17.29	–64:01:15.2	151.6(5)	3.5 / 4	8–9	–	–
MTP0049	14:05:37.10	–65:05:25.3	346.5(7)	8.1 / 9.2	9	–	–

[†]DM measured using DM_PHASE

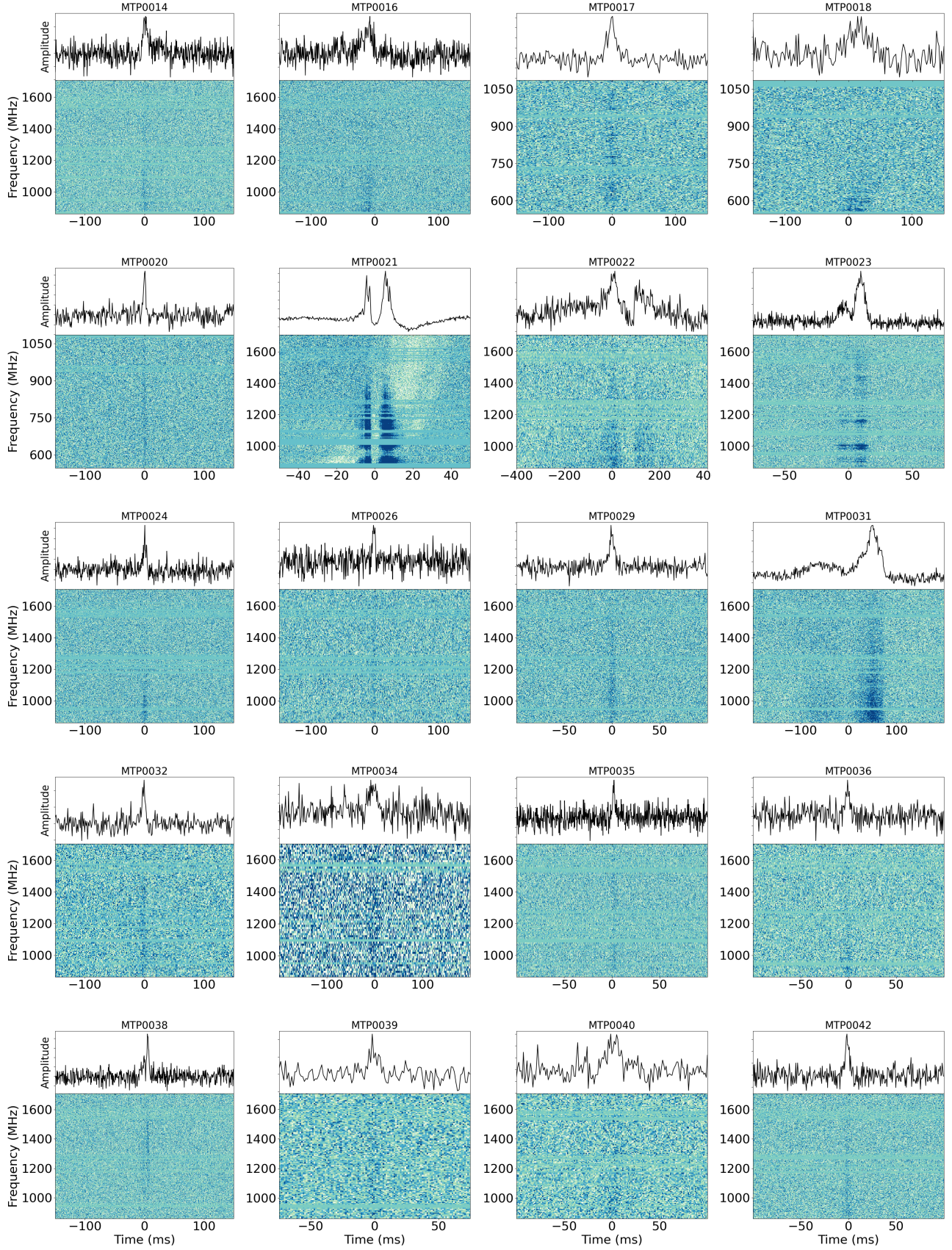


Figure 2. Dynamic spectra (bottom) and frequency-averaged pulse profiles (top) for the new Galactic transients. Each pulse shown is the first that MeerTRAP detected. These plots have been produced in the same way as in Figure 1. Some data have been downsampled in time to improve the visibility of the pulse. Blank horizontal lines are masked channels that were affected by RFI. The pulse of MTP0021 is visibly affected by flux over-subtraction due to zero-DM RFI removal.

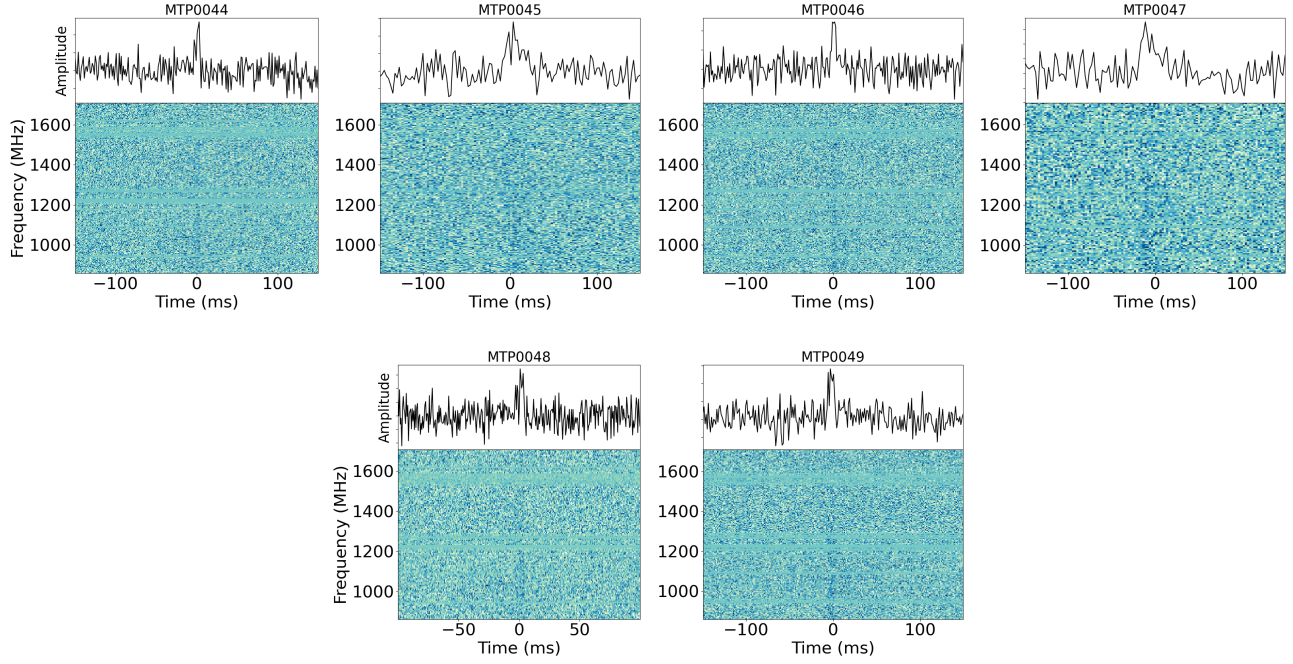


Figure 2. (continued)

Table 4. Timing solutions for the five RRATs; MTP0014, MTP0017, MTP0020, MTP0023 and MTP0034.

	Fit and data-set				
PSR name	J1911–2020	J0402–6542	J1930–1856	J1319–4536	J1108–5946
MeerTRAP name	MTP0014	MTP0017	MTP0020	MTP0023	MTP0034
MJD range	59301.3–60385.1	59214.8–60506.1	59324.1–59818.8	59369.8–60506.9	59513.5–60008.2
Data span (yr)	2.97	3.54	1.35	3.11	1.35
Number of TOAs	648	132	231	91	134
Rms timing residual (ms)	11	2.5	3.8	5.2	7.4
Weighted fit	Y	Y	Y	Y	Y
Reduced- χ^2	444	5.4	380	1400	17
Measured Quantities					
Right ascension, α (hh:mm:ss)	19:11:16.05(8)	04:02:52.27(3)	19:30:41.88(9) [†]	13:19:48.31(6)	11:07:58.56(23) [†]
Declination, δ (dd:mm:ss)	–20:20:02(9)	–65:42:43.41(16)	–18:56:28.5(12)	–45:36:03.0(8)	–59:47:01.1(12)
Spin period, P (s)	4.4679211203(2)	3.03352298461(7)	1.76083292621(3)	1.8709058202(2)	1.516531549(3)
First derivative of P , \dot{P} ($\times 10^{-15}$ ss $^{-1}$)	6.726(8)	5.601(2)	0.593(7)	6.975(3)	0.22(17)
Epoch of period determination (MJD)	60098	59581.5	59581.5	59369	60001.2
Epoch of position determination (MJD)	60098	59581.5	59581.5	59369	60001.2
Epoch of DM determination (MJD)	60098	59581.5	59581.5	59369	60001.2
Dispersion measure, DM (cm $^{-3}$ pc)	71.30(3)	31.5(2)	63.143(9)	40.41(8)	92.7(4)
Derived Quantities					
Characteristic age (Myr)	10	8.6	47	4.3	110
\log_{10} (Surface magnetic field strength, G)	12.7	12.6	12.0	12.6	11.8
\log_{10} (Spin-down luminosity, ergs/s)	30.5	30.9	30.6	31.6	30.4
Assumptions					
Clock correction procedure	TT(TAI)	TT(TAI)	TT(TAI)	TT(TAI)	TT(TAI)
Solar system ephemeris model	DE405	DE405	DE405	DE405	DE405
Binary model	NONE	NONE	NONE	NONE	NONE
Model version number	5.00	5.00	5.00	5.00	5.00

[†]Position is from an image localisation of transient buffer data, not from fitting in TEMPO2

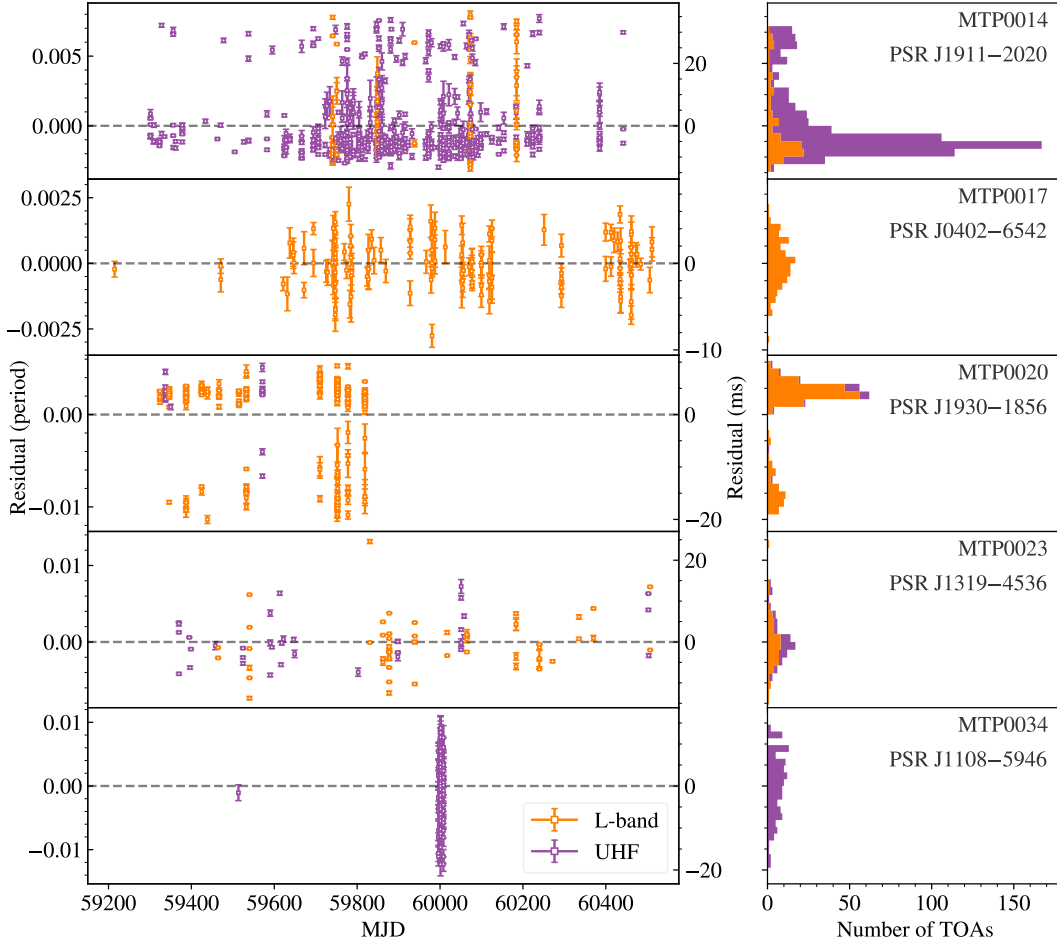


Figure 3. Residuals (*left panels*) and stacked histogram of residuals (*right panels*) from the best fit model given in Table 4 for the five sources with timing solutions.

On 2023 January 28, PSR J1911–2020 triggered the TB. We constrained the position using the resulting image from the data. We measured TOAs for all the pulses up to 2024 July 25 and, using the image localisation and initial period, were able to find a phase-connected timing solution spanning the three years of data. The resulting position fit of RA 19:11:16.05(8) and Dec $-20:20:02(9)$ is more constraining than the image localisation. In Figure 3 we show the timing residuals produced by subtracting the model-predicted arrival times from the measured TOAs. These are plotted for each observing frequency and their distribution is shown as a frequency-stacked histogram. The residuals reveal that PSR J1911–2020 has an average profile consisting of at least three components. Given our methodology of fitting a single Gaussian to the profile, we would expect a trimodal distribution of TOAs with each peak height reflecting the prevalence of each component. This is similar to the magnetar-like PSR J1819–1458 (Lyne et al. 2009; Bhattacharyya et al. 2018) where component flux variation produced three bands in the residual-space. Both PSR J1819–1458 and PSR J1911–2020 have a similar period but the period derivative of PSR J1911–2020 is ~ 100 times smaller, thus has a greater characteristic age by approximately 2 orders of magnitude greater. These calculations assume a dipolar magnetic field configuration. The leading component of PSR J1911–2020 is the dominant or only pulse visible for 76 per cent of the observed pulses, while the middle and trailing component each dominate 12 per cent. On 2022 January 3 at UTC 09:06:42 we detected the only

three component profile seen so far. This pulse closely resembles the residual distribution in that the leading component is more prominent and the three components are evenly spaced apart. Due to the dominance of the main component and the lack of structure evident in its residual distribution such as timing noise, the timing would not be improved by subtracting the offset between the residual bands as was the method of Bhattacharyya et al. (2018). Furthermore, timing noise is much less prominent in older pulsars (Hobbs et al. 2010). We have used the large number of detections to investigate the activity of PSR J1911–2020 further. Our calculations and analysis only use detections made after 2021 March 20 when targeted observations began. The average detection rate across these observations is 74 hr^{-1} , and split by observing band it is 68 hr^{-1} for L-band and 127 hr^{-1} for UHF. The rate at UHF is expected to be higher due to the pulsar spectral index. If we take a value of -1.6 (e.g. Jankowski et al. 2018), and assume that the difference in contribution due to the sky and receiver temperatures is small, we would expect a ratio between the rates of $(816/1284)^{-1.6} \times \sqrt{544/856} = 1.65$. Instead we observe a factor 1.88, which could be due to a slightly steeper spectral index, or observational effects such as the UHF band being generally cleaner than L-band, or due to the larger size of the UHF CB. We analyse the pulse detections in more detail in Figure 4. Panel A and B tally all observations of the primary target J1911–2006 and detections of PSR J1911–2020. In panel C, the cumulative targeted observation time, T_t against the cumulative number of detections,

$N_{\text{det,t}}$ shows that the detectability of PSR J1911–2020 increased after around MJD 59700. This does not appear to be solely the result of UHF detections increasing the mean rate, so we could be observing an increased detection rate from intrinsic changes at this epoch. In panel D, we show the histogram of detection rates. As alluded to in Section 2.3, we see the detection rate distribution is affected by the fact that J1911–2006 is a calibrator. Most observations are 120 s long, corresponding to 95 s of MeerTRAP time. The rate appears to be boosted at integer values of $N_{\text{det,t}}$ in this time frame. To investigate the nature of the wait times distribution in panel E, we use the same method as [Bezuidenhout et al. \(2022\)](#) to fit a modified Poissonian distribution. If the wait time, δ between detections that have an underlying pulsation rate, $r = 1/P$, was determined by a random process, then their probability distribution would be

$$\mathcal{P}(\delta | r) = r e^{-\delta r}. \quad (1)$$

An example of Poisson-distributed wait times is the giant pulses of the Crab pulsar (e.g. [Karuppusamy et al. 2010](#)). Other transient sources often exhibit non-random burst rates, instead being much more clustered in time. This includes some RRATs (e.g. [Shapiro-Albert et al. 2018](#); [Bezuidenhout et al. 2022](#)) but also repeating FRBs, for example FRB 20121102A ([Scholz et al. 2016](#)) and FRB 20201124A ([Lanman et al. 2022](#)). As [Oppermann et al. \(2018\)](#) shows, this can be parameterised by the Weibull function, which includes an extra shape parameter, k such that

$$\mathcal{W}(\delta | k, r) = k \delta^{-1} [\delta r \Gamma(1 + 1/k)]^k e^{-[\delta r \Gamma(1+1/k)]^k}, \quad (2)$$

where the gamma function, Γ is given by

$$\Gamma(x) = \int_0^{\infty} t^{x-1} e^{-t} dt. \quad (3)$$

For $k = 1$, the Weibull function returns to the Poisson-distributed exponential. We use the non-linear least-squares method of the PYTHON module `scipy.optimize.curve_fit` to fit the wait times, and show it overlaid on the distribution in [Figure 4](#). The fit returns the rotational frequency, $r = 1/P$ and $k > 1$ showing that the pulses are evidently more clustered than would be the case for randomness. The clustering is not a manifestation of a short observation bias, as we exclude durations longer than 120 s before the fit, as wait times longer than this are not sampled as often.

MTP0016/PSR J1525–2322

MTP0016/PSR J1525–2322 was detected during a MeerKAT commissioning observation on 2020 December 25, with the first pulse arriving at UTC 01:59:02. It was seen in one CB centred on RA 15:25:06.41 and Dec –23:22:19.1 and located on the edge of the area filled with CBs, but was not seen in the IB. Three more pulses were seen in the same beam over the subsequent 173 s. The pulses had S/N values of 8–14 and DM values between 38–42 pc cm^{−3}. Using `SCATFIT` we measured the best DM to be 41.2±0.3 pc cm^{−3}, which would place MTP0016 at 1.7 kpc (NE2001) or 3 kpc (YMW16). The nearest pulsar of a similar DM is PSR J1530–2114 at 2.5° away with DM 37.95 pc cm^{−3} ([Fiore et al. 2023](#)). The first pulse, shown in [Figure 2](#), has a hint of a precursor component, but the rest are single-peaked. With these four arrival times, we used `RRATSOLVE` to calculate a spin period of 5.5719(2) s. PSR J1525–2322 was detected in only the first of 16 separate 600-s observations of the primary target, which were spaced almost periodically across approximately 9 hours. The reason PSR J1525–2322 was not detected again when the target was revisited could be explained by its position at the edge of the first CBs. The PSF of the beams will change shape significantly

due to the changing availability of baselines and also their projected length in the direction parallel to the line of sight to the source as its elevation changes. It is possible that the elliptical beams rotated such that PSR J1525–2322 fell into a less sensitive part of the CB, and therefore could not be detected again. However, it could also be that the activity or flux density of the source dropped. The measured average detection rate of PSR J1525–2322 was therefore between 3.5 hr^{−1}–52 hr^{−1} depending on the length of time PSR J1525–2322 was actually detectable, but this cannot be determined until the source is localised further. PSR J1525–2322 is probably located fairly centrally within the CB, as there were no IB detections. Therefore, we provide the region bounded by the CB as a proxy for the positional uncertainty. Using a record of the antennas used and `MOSAIC`, we know the beam shape was 56″×27″ with an orientation of 290.8°²³. This field has not been revisited by MeerTRAP, so no more pulses have been seen since.

MTP0017/PSR J0402–6542

We first detected MTP0017/PSR J0402–6542 on 2020 December 31 at UHF during a 4 hour observation of the calibrator J0408–6545/B0407–65. Only one pulse, which is shown in [Figure 2](#), was seen. Targeted observations started on 2021 September 13, since then 133 pulses have been seen. The brightest pulse has a S/N of 19, for which we used `SCATFIT` to find a DM of 31.5±0.2 pc cm^{−3}. The low maximum S/N suggests that PSR J0402–6542 has a pulse energy distribution that is concentrated towards a relatively low luminosity. The height above the Galactic plane predicted by the DM distances are 1.0 (NE2001) and 1.8 (YMW16) kpc are the highest of the new sources. The mean detection rate across the targeted observations is ~ 1.4 hr^{−1}. This had initially made it difficult to obtain a period using `RRATSOLVE`, as we could not detect enough pulses during the short calibrator dwells. Eventually we were able to find a period of 3.03 s. On 2023 August 28, PSR J0402–6542 triggered the TB, which allowed us to get a position accurate to approximately 3″. Using the period and localisation, we found a long-term phase-connected timing solution using `TEMPO2`, which is provided in [Table 4](#). The characteristic age of about 9 Myr is consistent with PSR J0402–6542 being an RRAT. The timing position provides a factor of 20 improvement in the localisation precision compared to that provided by imaging. The residuals resulting from the timing model are shown in [Figure 3](#). The residuals are distributed quasi-randomly about zero, and the reduced- χ^2 from the weighted fit is relatively close to unity.

We have performed the same calculations of the long-term activity and detection statistics as we did for MTP0014. The calibrator J0408–6545/B0407–65 is the only primary target during which PSR J0402–6542 has been detected. The tally of observations and detections and the detection rate and wait time statistics are shown in [Figure 5](#). The steady increase in the cumulative observation time of the calibrator contrasts with the stepped cumulative detection count. The clusters of detections do not seem to be dependent on how often the calibrator is observed. It therefore appears that PSR J0402–6542 appears to enter epochs of increased activity approximately every 300 days.

²³ The shape is the semi-major and semi-minor axes, a , b and the angle is anti-clockwise starting from b pointed North in the J2000 world coordinate system. The size corresponds to when the sensitivity drops to 25 per cent of the maximum. Beam shapes and orientations throughout this article are in this format.

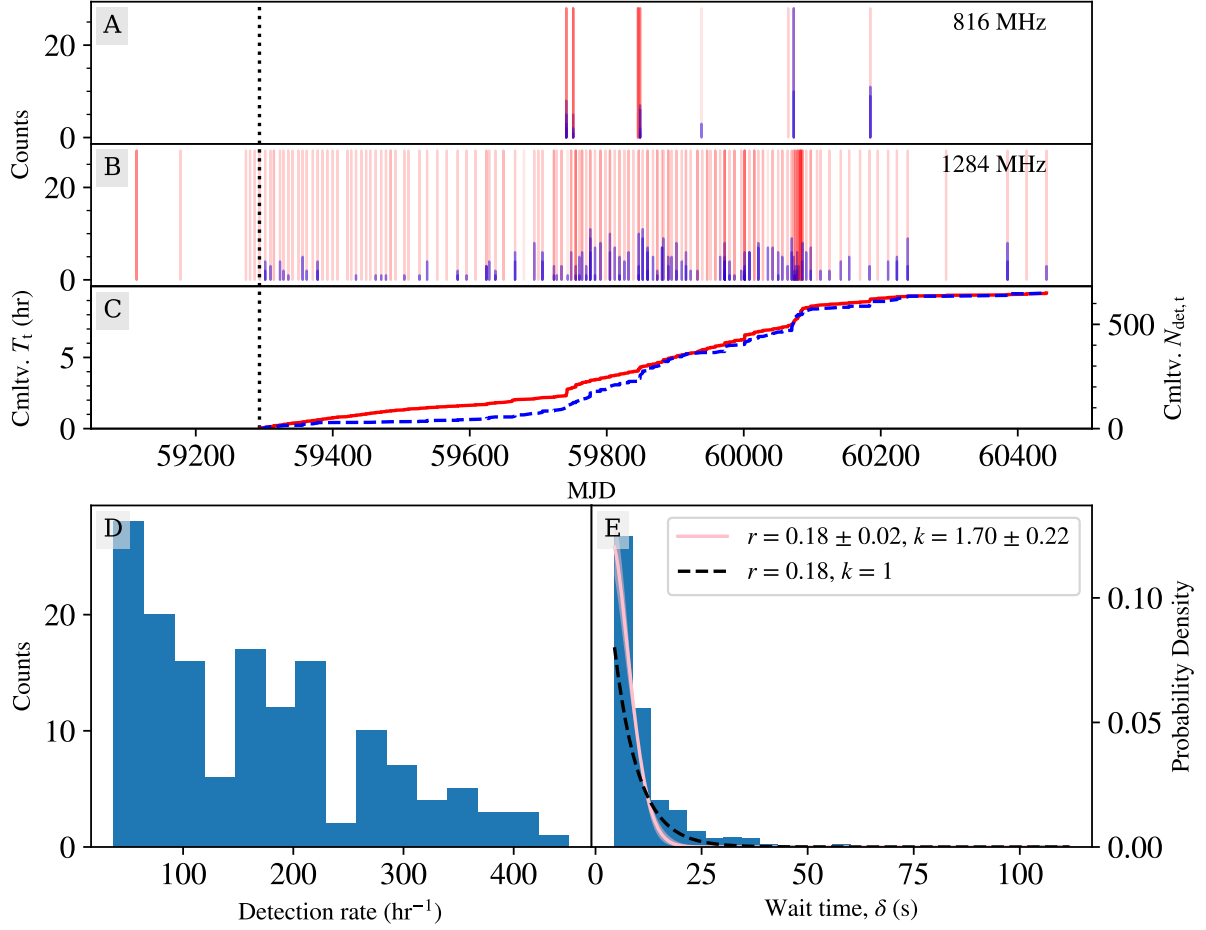


Figure 4. *Upper:* Plots tallying the integration time and number of detections of MTP0014/PSR J1911–2020 at UHF (A) and L–band (B). Red shaded boxes are extent of the observations of the primary target J1911–2006. The dashed vertical line marks the date that targeted observations began. Darker shades of red are an effect of plotting narrow shaded regions over a long baseline, so only signify that the calibrator was more frequently visited. Panel C shows the cumulative targeted observation time, T_{obs} as a solid line and the cumulative number of detections, N_{pulse} as the dashed line. *Lower:* Panel D: histogram of pulse rates calculated for all targeted observations. Panel E: histogram of the wait times, δ between consecutive pulses in targeted observations. The best-fit for $\mathcal{W}(\delta | k, r)$ and phase-space encapsulating the 3-sigma uncertainty of k and r are overlaid in pink, and the same function for $k = 1$ is shown as the dashed line.

MTP0018

MTP0018 was detected on 2021 January 1 as a single pulse in an incoherent beam centred on RA 04:08:20.38, Dec $-65:45:09.1$. The candidate had a DM of 28.55 pc cm^{-3} and S/N 8.5, but it was underdispersed due to being affected by short duration zero-DM RFI occurring during the arrival of the dispersed pulse. It was initially suspected that we had made an incoherent mode detection of MTP0017 due to the similar DM and the proximity of the IB to the positions of CBs where MTP0017 has been detected on both days either side. However, after robust cleaning of the data, we constrained the DM to $38.8 \pm 0.3 \text{ pc cm}^{-3}$, far from that of MTP0017. The pulse has a width of approximately 33 ms, wider than any pulse we have detected from MTP0017. The pulse flux is highly concentrated at the bottom of the band, and such a steep spectrum suggests a position far from the IB centre where the lower frequencies remain somewhat sensitive. Interestingly, MTP0018 has not been seen again since, despite approximately 1000 observations of the calibrator in the 4.5 years since this detection. This could be due to being positioned in a very low sensitivity part of the IB. Alternatively, MTP0018 could be a very infrequently emitting source, or has an unusual burst energy

distribution. We note that the DM slightly exceeds the maximum line of sight value predicted by the Υ_{MW16} model of 37 pc cm^{-3} , and close to the NE2001 value of 43 pc cm^{-3} . This raises the possibility that MTP0018 is located in the Galactic halo but likely not beyond given a predicted total halo contribution to the line of sight of $\sim 40\text{--}50 \text{ pc cm}^{-3}$ (Yamasaki & Totani 2020), making it unlikely MTP0018 is a one-off FRB. Such an event could however explain the low detection rate. MTP0018 is the only source to have exclusively been seen in a UHF IB.

MTP0020/PSR J1930–1856

This source was first detected on 2021 April 20 in a CB during an observation of the binary PSR J1930–1852 (Swiggum et al. 2015) as part of the MeerTIME project’s (Bailes et al. 2016) relativistic binary programme (Kramer et al. 2021). A multibeam localisation was performed using a simultaneous L–band detection in three CBs, and PSR J1930–1856 has been detected during every targeted observation since. The pulses are characterised as very narrow and predominantly single component, with a small fraction seen with two components. The DM from SCATFIT of $63.143 \pm 0.009 \text{ pc cm}^{-3}$

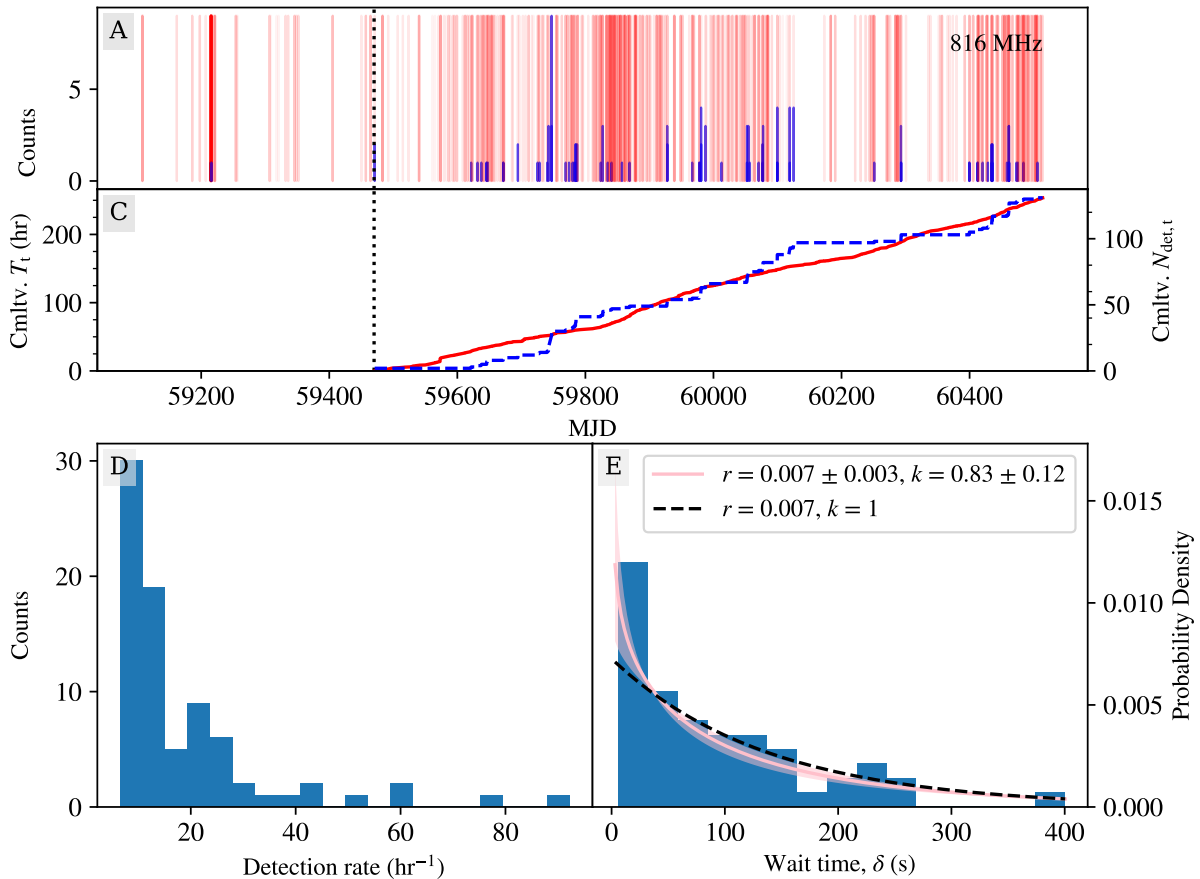


Figure 5. Observations and activity of MTP0017/PSR J0402–6542, where the contents of each panel are equivalent to those in Figure 4. Panel B is not present as there are no L-band detections of PSR J0402–6542.

is well constrained due to the small width and sustained brightness across the frequency band. The TB was triggered by a pulse on 2022 June 22, which allowed us to localise PSR J1930–1856 to an accuracy of approximately $1''$. We selected a bright pulse detected in a CB at UHF on 2022 June 22 for imaging and localisation of the PSR J1930–1856. We created the two images in Figure A1, "on" and "off", with each covering the same duration. We identified a transient source in the on-pulse image, as indicated by the magenta circle in Figure A1. Considering this source appears only at the time of the pulse detection and there is no other transient source in the image, we determine that this is PSR J1930–1856. Running `PYBDSF` on the astrometry corrected image, we found the source position to be RA 19:30:41.88, Dec $-18:56:28.49$. The total uncertainty after combining all uncertainties in quadrature was 1.3 arcsec in RA and 1.2 arcsec in Dec.

As with MTP0014 and MTP0017, we found a period using `RRATSOLVE` on a cluster of pulse arrival times, and used the localisation to fit a timing model in `TEMPO2`. The position could not be improved any further, thus was excluded from the fit. The resulting timing solution is given in Table 4. The \dot{P} of $(5.93 \pm 0.07) \times 10^{-16} \text{ s s}^{-1}$ gives a large characteristic age of 47 Myr. The residuals that result from the fit, shown in Figure 3, are distributed across two strips. Based on this and having not detected any pulses with three or more components, we infer that the integrated profile is double-peaked. The trailing component is often narrower, which is reflected in the smaller TOA uncertainties in the upper strip. Some residuals lie in

the gap between the strips, which we infer is the result of detecting PSR J1930–1856 as the emission switches between the two components. The Gaussian is fitted to both components at the same time and the uncertainties on these TOAs are larger due to the larger Gaussian widths. We demonstrate an example of this effect in Figure 6. Pulse (i) and (ii) are separated by three rotations, whereas pulse (ii) and (iii) are consecutive. The pulses have been aligned by shifting the time series by the timing residual value. We see that the amplitude of one pulse increases while the other decreases, rather than appearing stochastically and independently of each other.

The average detection rate of targeted observations is 25 hr^{-1} : 10 hr^{-1} at L-band and 26 hr^{-1} at UHF. The ratio between these of 2.6 is an even more pronounced departure from that expected based on nominal sensitivity that we calculated for MTP0014, but these rates are likely to be very uncertain, especially at L-band where there have been only 2 targeted observations. We repeated the analysis of detection statistics as for MTP0014 and MTP0017, and show the results in Figure 7. We do not show the detection tally due to the sparse cadence of targeted observations. The Weibull fit finds $k = 0.62 \pm 0.20$, which does not strongly suggest the pulses are any more clustered than randomness. There have been no observations of the primary target PSR J1930–1852, nor any detections of PSR J1930–1856 since 2022 August 27.

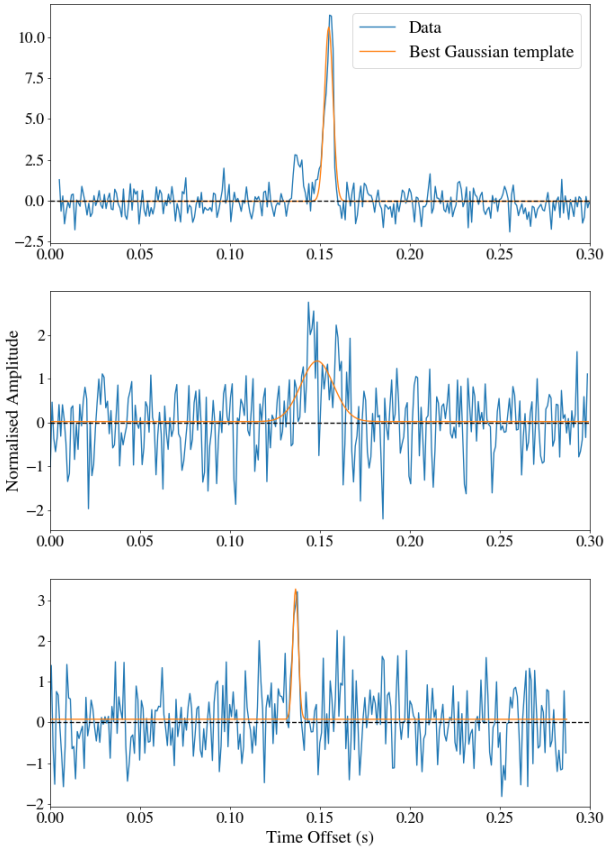


Figure 6. Plots showing three successive detections of pulses from MTP0020/PSR J1930–1856, overlaid with the best fit Gaussian from our timing method. From top to bottom: (i) a pulse of S/N 31 detected at MJD 59777.810276813 showing both the leading and trailing components of the average profile, (ii) the next detection three rotations later in time showing a pulse of S/N = 8 and possibly two components, where the best Gaussian fit is a wider profile centred approximately at their midpoint and (iii) the S/N = 8 pulse from next rotation showing the narrower leading component. The trailing component is no longer present.

MTP0021/PSR J0219–06

PSR J0219–06 was first detected in several CBs and the IB on 2021 April 26 as a series of 6 very bright pulses between S/N 27 and 134. PSR J0219–06 has the lowest DM of any MeerTRAP discovery at 8.46 ± 0.07 pc cm⁻³, which we obtained using `DM_PHASE`. It was detected at DM values above the 20 pc cm⁻³ threshold due to its brightness and prominent substructure. The pulses were brightest in the IB (the first pulse is shown in Figure 2) and there is no spatial cohesion between the five CBs, so those are very likely sidelobe detections. PSR J0219–06 should therefore be located in the region outside the area filled with CBs. The pulse profile consists of two components with microstructure present. The flux deficit around the pulse is an effect of the zero-DM filter removing mean channel values that have been boosted by the brightness of the pulse. This has caused the frequency-averaged flux to dip below the noise level. The observation, which was part of the MIGHTEE (MeerKAT International GHz Tiered Extragalactic Exploration; Taylor & Jarvis 2017) survey, lasted approximately 6 hrs. However, the pulses were all detected within 6 minutes. Using `RRATSOLVE` we find a period of 1.88 s, ruling out any possibility that this source is an LPT. Nevertheless, the pulse profile and frequency evolution bear a striking resemblance to those of the 76-second pulsar (Caleb et al. 2022a). There are also

similarities with the radio pulses of magnetars like XTE J1810–197 (Caleb et al. 2022b; Bause et al. 2024). The lack of a localisation has precluded multiwavelength follow-up observations thus far. The 20 pc cm⁻³ threshold explains why we only detected pulses of high S/N, as they had sufficient brightness to be seen at higher DMs. We likely missed a population of fainter pulses, unless PSR J0219–06 has an unusual burst energy distribution. The exceedingly low average detection rate of 0.6 hr⁻¹ should then serve as a lower limit. Both Galactic electron density models predict a distance of about 400 pc.

MTP0022

MTP0022 was discovered when two pulses were seen 189 s apart in a single coherent beam on 2021 May 10. The detections were during a MeerTIME observation of the binary pulsar PSR J1244–6359 (Ng et al. 2015). The first pulse seen is shown in Figure 2 and happens to be the brightest. We used `DM_PHASE` to measure a DM of 342 ± 2 pc cm⁻³. The pulse is very wide at 0.2–0.3 s towards the bottom of the frequency band, suggests a long rotational period of perhaps several seconds. MTP0022 is probably located within the CB, so the positional uncertainty is defined by the beam shape, which was $55'' \times 37''$ at an angle of 17.8° . MTP0022 has not been seen again in approximately 49 minutes of targeted observations of PSR J1244–6359.

MTP0023/PSR J1319–4536

The first pulse detected from MTP0023/PSR J1319–4536, shown in Figure 2, was on 2021 June 4 at L–band. It was bright enough to be detected with a S/N of 18 in the IB and the sidelobes of six CBs. Several more pulses were detected in the IB over ~ 3 hours, which allowed us to derive a period of 6.18 s using `RRATSOLVE`. We have since detected a population of nearly 100 pulses from this source, exclusively during observations of the gain calibrator J1318–4620 | 1315–46. We find a diverse set of pulse shapes; some pulses are singly peaked, some show multiple components and some also or exclusively exhibit microstructure. To measure the DM, we ultimately used `DM_PHASE` with a bright multi-component pulse rather than the outright brightest pulse which was single peaked. The profile and dynamic spectrum of the pulse used is shown in the lower plot of Figure 8, which has three main components and some microstructure, and returns a DM of 40.41 ± 0.08 pc cm⁻³. The average detection rate across targeted observations at UHF is 26 hr⁻¹, similar to that of MTP0020. They also share similar spin periods and both have high pulse-to-pulse variability. PSR J1319–4536 has been detected independently by the CRACO project (Wang et al. 2024). During observations for the Evolutionary Map of the Universe (EMU; Norris et al. 2021) survey at 799.5–1087.5 MHz, Wang et al. (2024) detected 20 pulses in a total of 10 hours. The period, DM and position they inferred from their detections are consistent MeerTRAP’s measurements.

We were able to localise PSR J1319–4536 using `SEEKAT` for a UHF multibeam detection. The threshold on the angular distance from the primary target for a targeted CB to be deployed is the size of the IB at the middle of the band. PSR J1319–4536 lies within the UHF IB but not the L–band IB, therefore it has only targeted during UHF observations. The detection rate and wait time statistics of these observations are shown in Figure 7. The Weibull fit to the wait times has a large uncertainty but the best fit is almost consistent with the Poissonian case of $k = 1$. A UHF CB detection of PSR J1319–4536 on 2024 May 13 triggered the TB, which improved the positional uncertainty down to just $1.3''$. Ultimately we achieved a precision

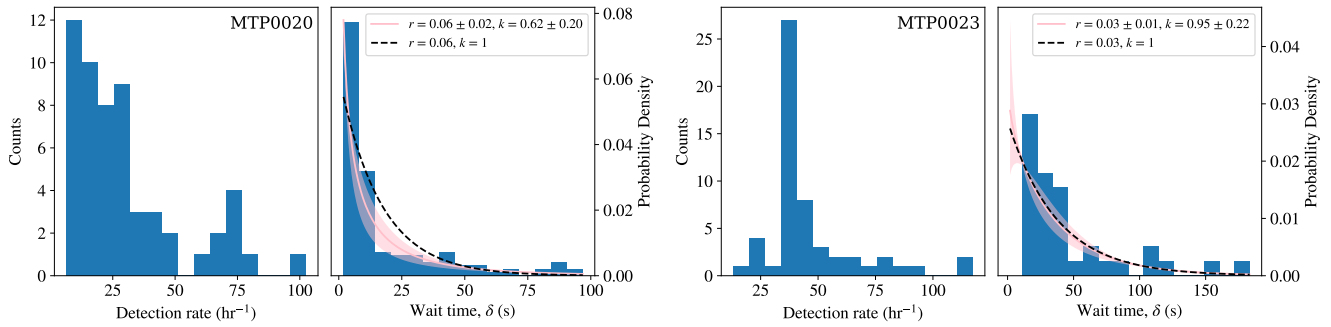


Figure 7. Rates and wait time statistics of targeted detections of MTP0020/PSR J1930–1856 (L–band and UHF) and MTP0023/PSR J1319–4536 (UHF). These have been calculated in the same way as for Figure 4.

of $<0.1''$ by fitting a timing solution, which is provided in Table 4. From the measured \dot{P} of $6.97 \times 10^{-15} \text{ s s}^{-1}$ we find PSR J1319–4536 to be the youngest of the five RRATs we have timed at an age of ~ 4 Myr, and that of the largest spin-down luminosity.

PSR J1319–4536 also often exhibits extremely variable emission across the frequency band characteristic of diffractive scintillation by the interstellar medium. In the upper plot of Figure 8, we show a similar triple-peaked pulse to that in the lower plot that was detected nearly 2 years later in the IB at L–band. The frequency overlap between L–band and UHF makes clear the increasingly wide scintillation bandwidth at higher frequencies. The scintillation bandwidth, $\Delta\nu_s$ is defined as the frequency width of a scintle, and relates to the scattering timescale, τ_s of the pulse as $2\pi\Delta\nu_s\tau_s \sim 1$ (Cordes & Rickett 1998). We were unable to measure τ_s , so instead we estimate its value using the empirical dependence on DM derived by Lewandowski et al. (2015). Using these relations, we find the predicted values to be ~ 12 MHz at 816 MHz and ~ 70 MHz at 1284 MHz, which appear to agree with the flux variation visible in these pulses. We note the very sharp drop in flux above 1400 MHz which differs from the L–band IB discovery pulse in Figure 2, where emission can be seen above this frequency. PSR J1319–4536 is located just beyond the edge of the L–band IB, so the frequency dependence of the IB size results in a drop in sensitivity at higher frequencies. We suspect the presence of the sharp cut-off is a combination of an intrinsically weaker pulse with stronger amplification in scintillation bands below 1400 MHz. We have also analysed the microstructure and see strong evidence that it has a periodicity. In Figure 9 we show the frequency-integrated profile of a pulse consisting solely of micropulses seen on 2022 October 25. We also show the autocorrelation function (ACF) of this profile. The periodicity of 5 bins or 2.4 ms compared to the spin period agrees very well with the empirical relation found by Kramer et al. (2024) which predicts a micropulse periodicity of $\sim 0.001P$. The same periodic microstructure is also visible in the pulse in the lower plot of Figure 8.

MTP0024

MTP0024 was detected on 2021 June 7 and 8 during a TRAPUM (Stappers & Kramer 2016) observation of the accreting millisecond pulsar SAX J1808.4–3658. We show the first pulse in Figure 2 for which we find a DM of $41.0 \pm 0.5 \text{ pc cm}^{-3}$ with SCATFIT. The detection was in the IB only which makes it certain that the emission does not originate from SAX J1808.4–3658. Two pulses were detected, each during the second and third of three 1 hr observations a day apart. This observation block was repeated in May 2022 but MeerTRAP did

not see any more pulses. Across the six observations, the detection rate for MTP0024 is therefore approximately 0.3 hr^{-1} .

MTP0031/PSR J0917–4245

MTP0031/PSR J0917–4245 was detected in two CBs and the IB during an L–band observation of the Vela Supercluster on 2021 August 22. It was later detected in multiple CBs simultaneously during a later MMGPS–L observation, which enabled a multibeam localisation using SEEKAT. In addition, there were enough pulses detected to measure a spin period of 2.55 s using RRATSOLVE, inferring PSR J0917–4245 to be an RRAT. The pulses are predominantly composed of a main peak preceded by a weaker component of similar width, with a total on-pulse region of ~ 200 ms. The first pulse shown in Figure 2 shows this structure. The pulse shape has been seen to evolve; the precursor is occasionally brighter than the main peak, and the brighter pulses show a multi-peaked structure within the two components. Using the brightest of these, we measured a DM of $97.7 \pm 0.3 \text{ pc cm}^{-3}$ using DM_PHASE. We later saw PSR J0917–4245 in the IB of three other MMGPS–L observations where the IB was overlapping this position. The TB was triggered during the most recent of these on 2022 July 10 in the L–band IB. The position from SEEKAT was extremely useful for confirming PSR J0917–4245 in the wide-field image for two reasons. Firstly, the time difference between the images required by such a broad pulse was large. Then, even though the image S/N is boosted being an IB detection, the pulse had a low time-domain S/N of 8.3. The astrometrically corrected image position is RA 09:17:28.30, Dec $-42:45:54.51$ with an uncertainty of 1.2 arcsec in both RA and Dec. The on and off images can be found in Figure A1. We have also detected four pulses from PSR J0917–4245 during UHF timing observations of the MMGPS–L discovered pulsar PSR J0917–4413. We have not been able to target PSR J0917–4245 with a dedicated CB as it has always been just beyond our angular offset threshold set by the size of the IB. Thus we calculate a non-targeted detection rate of 12 hr^{-1} , though this is not a totally reliable value due to the different angular offsets from the primary target when detections were made. As of now, the long gaps between detections have prevented us from obtaining a phase-connected timing solution.

MTP0034/PSR J1108–5946

The new RRAT MTP0034/PSR J1108–5946 was discovered when a single pulse was detected in the IB of a MMGPS–L observation on 2021 October 26. The pulse, shown in Figure 2 had been detected at a

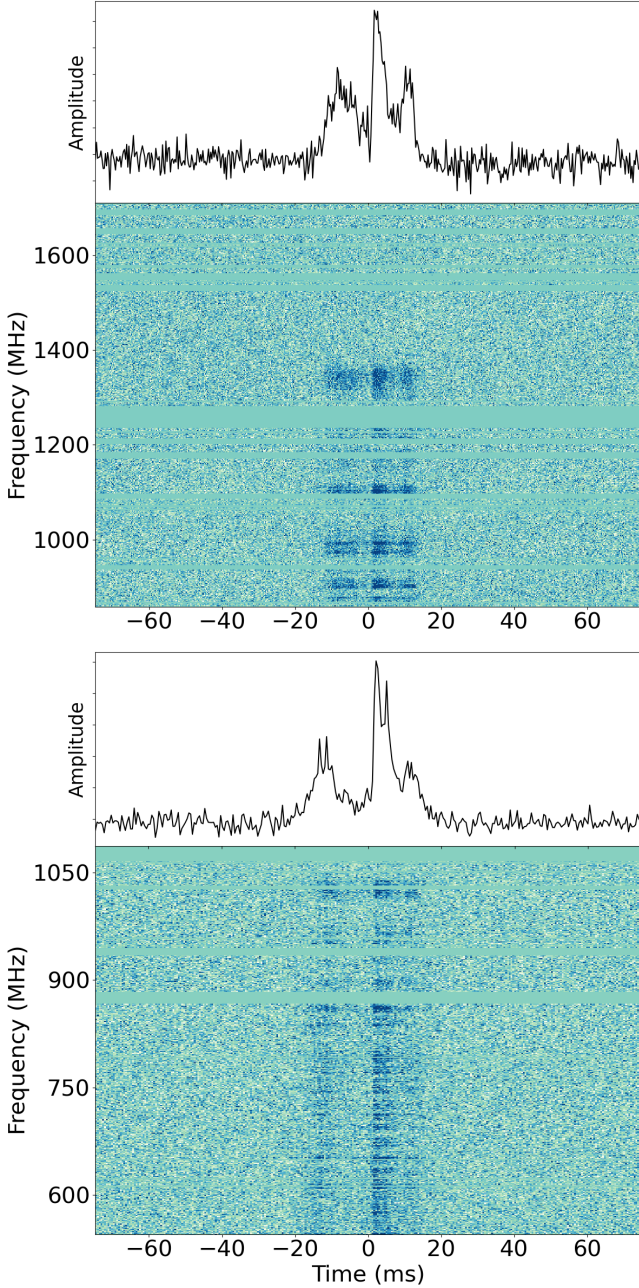


Figure 8. Dynamic spectra (bottom) and frequency-integrated pulse profiles (top) of two pulses from PSR J1319–4536: a UHF CB detection on 2022 October 10 (lower plots) and an L-band IB detection on 2024 June 11 (upper plots). The data were dedispersed at a DM of 40.41 pc cm^{-3} . The blank horizontal lines are masked channels that were corrupted by RFI.

S/N of 8.5. Then in February and March of 2023, 134 pulses were detected in CBs and the IB on three separate days. These were 15-minute L-band observations of a nearby X-ray binary system HD96670 by ThunderKAT (Fender et al. 2016). We used the brightest of these to measure the DM with SCATFIT to be $92.7 \pm 0.4 \text{ pc cm}^{-3}$. Using RRATSOLVE and a cluster of pulses seen at L-band on 2023 February 26, we measured a spin period of 1.52 s. During this same observation, the TB was triggered twice. We localised PSR J1108–5946 to RA 11:07:58.56, Dec $-59:47:01.10$ with an uncertainty of 1.8 arcsec and 1.2 arcsec in RA and Dec, respectively, using the voltage data

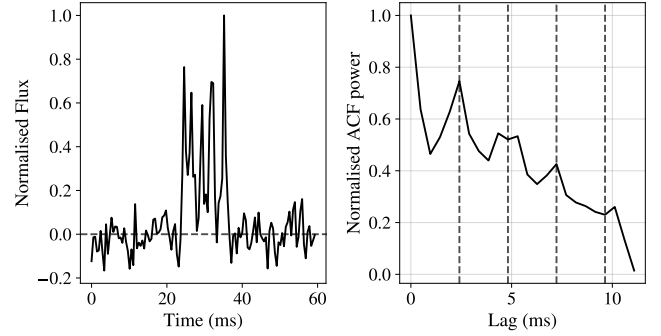


Figure 9. Baseline-subtracted and frequency-integrated pulse profile (left) from PSR J1319–4536 on 2022 October 25 and the autocorrelation function of the profile (right). The first dip in the function’s power is at the $\approx 1 \text{ ms}$ width of the micropulses and the periodicity of 2.4 ms, or 5 time samples, is shown as a dashed line which line up with the function peaks.

of the brightest detection. See Figure A1 for the on and off images of this source. The remarkable detection rate averaged across these observations is 160 hr^{-1} , the largest of all of the reported transients. PSR J1108–5946 was detected during all four observations, but we reiterate the caveat in Section 2.3 that any non-targeted detection rates serve only as an upper limit given there may be other nearby targets observed where no pulses were seen. HD96670 is approximately 15 arcmin closer to PSR J1108–5946 than the IB of the discovery MMGPS–L observation, which would explain why we observed a lower detection rate in the MMGPS–L IB.

We calculated TOAs for all the pulses and, using the image localisation and the spin period, we were able to fit a more accurate period across the ThunderKAT observations in TEMPO2. It appears that the large number of TOAs delivered a period accurate enough to phase-connect the first detection 500 days prior. We included the period derivative in the fit to obtain a $2.2 \times 10^{-16} \text{ ss}^{-1}$ significant to only 1-sigma. Detections spanning a greater length of time will be needed to constrain \dot{P} further. We suspect that the true \dot{P} is below the best fit value, as the inferred characteristic age is perhaps unreasonably high. We checked how much the \dot{P} measurement could be affected by apparent spin period variation due to the Earth’s orbital motion and an erroneous position. Assuming the RA uncertainty of 1.7 arcsec is the same in celestial coordinates, the maximum possible change in spin period is $0.8 \mu\text{s}$. This would change \dot{P} by $5.2 \times 10^{-17} \text{ ss}^{-1}$, which is smaller than the uncertainty of our measurement. The size of our uncertainty on \dot{P} ultimately limits how we can characterise PSR J1108–5946, though we have constrained it to be within the RRAT population.

MTP0035

On 2021 October 26 we discovered MTP0035 during a MMGPS–L observation. Two pulses of S/N 12.3 were detected in quick succession in the IB with DM values of 224–225 pc cm^{-3} . The first is shown in Figure 2, and we used SCATFIT to measure a DM of $224.5 \pm 0.2 \text{ pc cm}^{-3}$. The pulses are separated by $3.9548 \pm 0.0003 \text{ s}$, thus the period could be any integer factor up to this value. The position is still very uncertain as the source has not been detected in coherent mode nor has it triggered the TB.

MTP0039/PSR J1533–5609

MTP0039/PSR J1533–5609 was first detected on 2021 December 11 at UTC 04:27:02 during an L-band observation of the galaxy PGC3097177 (HYPERLEDA; Patel et al. 2018). Over the duration of approximately 7 hours a total of 31 pulses were seen in CBs only. The first of these is shown in Figure 2. PSR J1533–5609 was then detected 9 days later during a repeat of the observation block. We measured a DM of 95.31 ± 0.09 pc cm⁻³ using SCATFIT for the brightest pulse which had a S/N of 36.5 measured with SPYDEN. The spin period was calculated using RRATSOLVE for clusters of pulses from both observations and a consistent value of 1.06 s was found. We could not perform a multibeam localisation, as there is no instance of a single pulse of PSR J1533–5609 being detected in more than one CB. This is peculiar as there have been several pulses of S/N > 15 in beams of varying positions and orientations, so one might expect two beams to have coincidentally overlapped at the true position. This suggests that PSR J1533–5609 is located in the middle of these CB positions. In any case, PSR J1533–5609 has not been seen since the TB began operating, precluding an image-based localisation. We therefore provide a crude estimate of the position uncertainty as the region covered by the CB of the brightest pulse. This beam was located at RA 15:33:50.46 and Dec -56:09:29.7 and had a shape and orientation of 57''×40'' and 345.8°. Since these detections, MeerTRAP has targeted this position 14 times, but no detections have been seen in ~22 minutes. The average detection rate of the non-targeted observations is about 4.7 hr⁻¹. If we consider the burst rate to be a random process, this gives an uncertainty of 2 detections per hour which is consistent with rates too low to expect a detection in 22 minutes.

MTP0042

MTP0042 has only been detected during a MMGPS–L observation on 2021 October 08. Two pulses were seen in a single CB. We used the brightest of these to find a DM of 250.4 ± 0.7 pc cm⁻³ with SCATFIT. The closest pulsar on the sky with a similar DM is PSR J1621–5039 at more than 3° away. MTP0042 is likely located within the CB, which was positioned at RA 16:41:39.43, Dec -51:09:00.8 with a size of 46''×25'' and orientation of 8.5°. We calculated the difference in time between the TOAs of the two pulses to be 5.5143(5) s, and thus set this as the upper limit on the spin period where, as with MTP0035, any integer factor up to and including this value is also valid.

MTP0044/PSR J2218+2902

MTP0044/PSR J2218+2902 was discovered on 2022 January 02 during a UHF observation of the radio source J2218+2828, as part of the MeerKAT Absorption Line Survey (MALS; Gupta et al. 2016). 9 pulses were seen during approximately 110 mins, with DM values of 54–56 pc cm⁻³. The first is shown in Figure 2 and is also the brightest. With SCATFIT we fit a refined DM of 55.8 ± 0.4 pc cm⁻³. Using RRATSOLVE and the TOAs for all pulses, we find the best solution of the period is 17.49616(4) s. PSR J2218+2902 has therefore the third slowest spin period of a confirmed radio-emitting NS, behind the 23.5 s PSR J0250+5854 (Tan et al. 2018) and the 76 s PSR J0901–4046 (Caleb et al. 2022a). More detections are required to confirm the period. MALS had earlier observed the same source with the L-band receivers on 2020 September 02, but unfortunately MeerTRAP was not commensally observing that day. We have used eight of the pulses to attempt a localisation. Eight,

instead of all nine pulses were chosen because they are of a single component, so their S/N values are more reliable. We used MOSAIC to simulate the CB PSFs and combined them to form an average PSF weighted by the S/N of the respective pulse. We take the maximum of the average PSF to be the best position to be RA 22:18:23.3(19), Dec +29:02:56(33). This should be treated as an average position. The pulses can be grouped into two types; three have broader single-component profiles and six only have one or more narrow subpulses. Interestingly, the DM exceeds the maximum line of sight value of the γ MW16 model of 52.9 pc cm⁻³. The DM of the Galactic pulsar PSR J2222+2923, which is approximately 1° away, does not exceed either model (Deneva et al. 2024) but is within 3 DM units. PSR J2218+2902 is probably a Galactic source, potentially in the inner Galactic halo unless the electron content is underestimated in this region. We note that its positional uncertainty overlaps the centre of the galaxy cluster RM J221826.6+290308.6 (Rykoff et al. 2014), located approximately 46 arcsec away.

MTP0045/PSR J1531–5557

MTP0045/PSR J1531–5557 was detected at L-band on 2021 December 20, during the same observation of the galaxy PGC3097177 during which MTP0039 was seen for the second time. 28 pulses from MTP0045 were detected, and we used the brightest of these to refine the DM to 56.6 ± 0.8 pc cm⁻³ using SCATFIT. A period of 2.92 s was calculated using RRATSOLVE. PSR J1531–5557 was detected again on 2024 May 07 at L-band during the only targeted observation since discovery. One pulse was seen in the central CB of the targeted area, which is consistent given the mean detection rate from the discovery observation of ~1 hr⁻¹. This pulse triggered the TB, so we localised PSR J1531–5557 using the voltage data to RA 15:31:07.98, Dec -55:57:28.53 with an uncertainty of 1.4 arcsec in RA and 1.5 arcsec in Dec. For the on and off images of this source see Figure A1.

MTP0047

MTP0047 was first detected as a faint pulse of S/N=8.3 on 2022 January 16 at UTC 11:18:11 during a MeerTIME observation of PSR J1806–1154. The DM refined by SCATFIT is 152.4 ± 0.4 pc cm⁻³. MTP0047 has been seen again during observations of PSR J1806–1154; one pulse was seen between two non-targeted observations, and six pulses during the nine subsequent observations where MTP0047 was targeted by MeerTRAP. The pulses are all similar in width and frequency dependence as the discovery pulse in Figure 2. The targeted detection rate of ~21 hr⁻¹ is similar to the other new RRATs MTP0020 and MTP0023. The positional uncertainty we can infer is from the discovery beam, which was centred on RA 18:07:10.36, Dec -11:51:08.2 with a shape of 63''×43'' angled at -49.3°. We noticed a small peak approximately 0.705(2) s after the pulse detected on 2022 February 19. The feature has a S/N of 5, thus it is not sufficient to claim this separation to be the upper limit on the spin period. However, we note that the two closest pulses were detected 31.850(2) s apart, which would be consistent with 45 rotations to 2-sigma.

Nine additional sources of single epoch detections

Some of the new sources have one or a small number of detections and were seen during just one observation. We are therefore not able to infer much about their properties, but provide a summary

of these nine sources here in the order they were seen. During an MMGPS–L observation on 2021 June 25 at UTC 23:05:54, we detected MTP0026 as a faint pulse with a S/N ratio of 7.9. The S/N measured with SPYDEN rises to 9.8 when the data are dedispersed at the SCATFIT-refined DM of 206.8 pc cm^{-3} . The two DM-predicted distances disagree by nearly 3 kpc, but nonetheless both would place this source at hundreds of parsecs above the Galactic plane, thus not dissimilar environments. The dedispersed pulse, shown in Figure 2 is narrow at approximately 4 ms wide. It is visible across the frequency band, so the source is most likely located within the CB in which it was detected. The shape of the beam was $32'' \times 24''$ and orientated at an angle of 366.3° .

MTP0029 was also discovered during an MMGPS–L observation on 2021 August 20. Three pulses were seen 253 s apart with DM values between $201\text{--}202 \text{ pc cm}^{-3}$. The first pulse was the brightest at S/N 13.9 and was detected at UTC 21:46:33 and is shown in Figure 2. We refined the DM to 201.4 pc cm^{-3} using SCATFIT on this pulse. The CB was centred on RA 16:48:36.46 and Dec $-51:42:46.5$, which had a shape of $71'' \times 38''$ at an angle of 5.5° . The first pulse was also seen at S/N 10.9 in an adjacent beam. A minimum of three beams are required for a robust multibeam localisation. In this observation, Padmanabh et al. (2023) discovered the pulsar PSR J1650–5025 at a similar DM of 213 pc cm^{-3} . MTP0029 was seen in a CB 78 arcmin from their pulsar position, and a topocentric period of 59.6 ms does not connect the TOAs we measure for the MeerTRAP pulses. We therefore exclude the possibility that these pulses originate from PSR J1650–5025.

MTP0032 was detected as a single pulse during an MMGPS–L observation on 2021 October 12. Similar to MTP0026, the S/N was 7.9. The S/N is boosted to 11.0 after better RFI cleaning and when dedispersed at the SCATFIT-refined DM of 271.5 pc cm^{-3} . The beam was $38'' \times 24''$ in size, oriented at 336.7° and centred on the coordinates RA 14:52:34.91 and Dec $-62:35:06.0$. As can be seen in Figure 2, the pulse is consistently bright across the band. Even though we do not know the intrinsic pulse spectrum, it remains more likely that MTP0032 is located within the defined beam shape, rather than in a sidelobe.

We detected MTP0036 on 2021 October 30 at UTC 01:20:14 during an Open Time observation of the Vela Supercluster at L–band. The pulse was seen in a CB with RA 10:00:58.60, Dec $-51:45:52.9$, a size of $44'' \times 26''$ and an orientation of 355.4° . Using SCATFIT, we find measure the DM to be 128.9 pc cm^{-3} . The pulse, shown in Figure 2 has a S/N of 9.4, a width of ~ 5 ms and broadens at lower frequencies. The distances of 3.1 kpc (NE2001) and 0.4 kpc (YMW16) predicted by the DM are very discrepant. If we assume MTP0036 is an old pulsar/RRAT then it could be far above the Galactic plane, which would suggest the YMW16 distance of 3.1 kpc is more realistic. The non-targeted detection rate of $\sim 18 \text{ hr}^{-1}$ is high amongst the new sources, but the time on source of only 200 s is too low to conclude if this is indeed a representative value of the intrinsic activity.

MTP0038 was detected during a 1 hour MeerTIME observation of the relativistic binary pulsar PSR J1727–2946 on 2021 December 9 at UTC 06:12:24. The CB position was RA 17:27:25.11, Dec $-29:42:20.6$, the shape was $55'' \times 26''$ and the orientation angle was 339.4° . The pulse, shown in Figure 2 is dedispersed at the DM of 126.7 which we obtained with SCATFIT. The pulse has an interesting frequency dependence. The flux is concentrated at the centre of the band. This is unlikely to be due to MTP0038 being located in a sidelobe of the CB because we would expect an IB detection and much more rapid frequency evolution of the flux. Instead, we suggest the frequency dependence could be explained by scintillation. We note the similarity of the frequency evolution to those of bursts

seen from repeating FRBs, for example FRB 20240114A (Tian et al. 2024; Kumar et al. 2024). We attempted to use the sharpness of the trailing edge to fit for DM using DM_PHASE, but the S/N was not sufficient, even when the data were downsampled in time. We did not detect MTP0038 in the other four L–band observations of PSR J1727–2946 totalling ~ 4 hours, or in ~ 10.8 hours of observations at UHF. The average detection rate then is 0.6 hr^{-1} , though more observations would be required to confirm if this is due to a constant and intrinsically low activity or due to a highly variable burst rate.

MTP0040 was detected in a CB with S/N=9 during a MMGPS–L observation on 2021 December 16. Using SCATFIT the DM was refined to $264 \pm 1 \text{ pc cm}^{-3}$. The position, shape and orientation of the beam was RA, 13:57:49.48 and Dec $-65:07:40.7$, $38'' \times 28''$ and 327.4° respectively. Since its discovery, MeerTRAP was able to target this position briefly on 2024 February 17, but no pulses were detected in 94 ± 13 s.

MTP0046 was discovered on 2022 January 15 at UTC 10:20:15. This was detected during a MMGPS–L observation, in a CB centred on RA 15:58:46.25, Dec $-48:38:48.4$ and of size and orientation of $34'' \times 24''$ and 344.2° . We have refined the DM of the pulse using SCATFIT to $254 \pm 1 \text{ pc cm}^{-3}$. The pulsar PSR B1557–50 has a very similar DM, but is 2.1° away. The pulsar PSR J1554–4854 was discovered by (Padmanabh et al. 2023) during this observation, and has a DM of 255.6 ± 0.3 fully consistent with that of MTP0046. However, the position of the pulsar is 46 arcmin away from the beam MTP0046 was detected in. The frequency evolution of the pulse does not suggest that MTP0046 is a sidelobe detection of either PSR J1554–4854 or PSR B1557–50, therefore we conclude that this is a new source.

MTP0048 was seen as two pulses detected on 2022 February 03 in a single CB. The position of the beam was RA 14:29:17.29, Dec $-64:01:15.2$, the shape was $30'' \times 24''$ and the orientation was 311.3° . We used SCATFIT to find a DM of $151.6 \pm 0.5 \text{ pc cm}^{-3}$, which is consistent with PSR J1446–6405 which was discovered by Padmanabh et al. (2023) in the same observation. However, they localised the pulsar to a position 48 arcmin away and the spin period of 9 ms is shorter than the on-pulse region of the MeerTRAP pulses. Therefore we are confident that these are different sources.

Finally, MTP0049 was discovered when a single pulse was seen on 2022 February 06 in a CB with the shape $39'' \times 25''$ and orientation of 327.5° . Using SCATFIT we measured the DM to be $346.7 \pm 0.7 \text{ pc cm}^{-3}$, which is the largest of all the new sources presented here. The observing block was repeated about 4 months later, but no detections of MTP0049 were made.

4 DISCUSSION

4.1 The MeerTRAP population

MeerTRAP has discovered these new sources on a better than monthly cadence, highlighting the importance of such commensal observations. The ability to piggy-back on a diverse set of MeerKAT observations has provided discoveries with a diverse set of properties. In the past, there has been a bias towards discovering RRATs of higher DM due to many previous single pulse surveys focusing on searching the Galactic plane. The sky coverage away from the plane where the line of sight electron content is low has increased the likelihood of discovering low DM sources such as MTP0020, MTP0021 and MTP0044. Long integration times provided by the repeated coverage of primary targets such as calibrators, or of deep field imaging, allow more intermittent sources to be detected. Such sources are often missed by more uniform yet shallower single pass

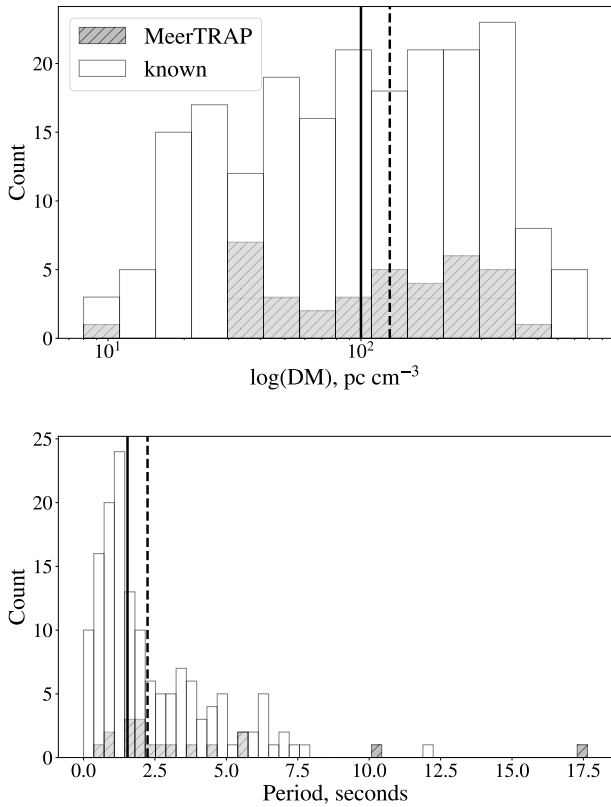


Figure 10. *Upper:* Histogram of the DM values of the Galactic transients discovered by MeerTRAP (shaded), compared to those of the rest of the RRAT population (un-shaded). The dashed line is the median value of the MeerTRAP DMs and the solid line is that of the known RRATs. *Lower:* Same for the period values of known and the new RRATs. Data for the non-MeerTRAP RRATs is from v2.2.0 of the ATNF Catalogue (Manchester et al. 2005).

surveys. Nevertheless, a plurality of 12 sources were seen during observations of the MMGPS–L survey. Due to its focus on the Galactic plane, MMGPS–L has provided the opportunity to sample more distant RRATs than previous surveys, further helped by the high instantaneous sensitivity of MeerKAT. Of these 12 sources, two are IB detections so would not have been visible in their survey at the time we saw them. Of the 10 CB discoveries, eight were not detected by the pulsar searching pipeline. This demonstrates and reinforces the distinguishing property of RRATs and the prediction by Cordes & McLaughlin (2003) that some periodic sources will only be detectable in single pulse searches.

Interestingly, the fraction of new RRATs discovered by commensal searches on the Galactic Plane Pulsar Snapshot (GPPS; Zhou et al. 2023) survey with the Five-hundred meter Aperture Spherical Telescope (FAST; Li & Pan 2016) compared to pulsars was $76/566 = 0.12$ at the time they were reported²⁴. This is similar to the equivalent fraction for our detections and MMGPS–L pulsar discoveries of $10/78 = 0.13$. This is clearly an important consideration for future pulsar searches that commensally searching for single pulses boosts the discovery yield by over 10 per cent. Interestingly, despite advances in survey sensitivities, RRATs continue to be found at a slower rate than normal pulsars, despite their larger predicted population (e.g. Keane & Kramer 2008).

²⁴ <http://zmt.bao.ac.cn/GPPS/v2.11.0>

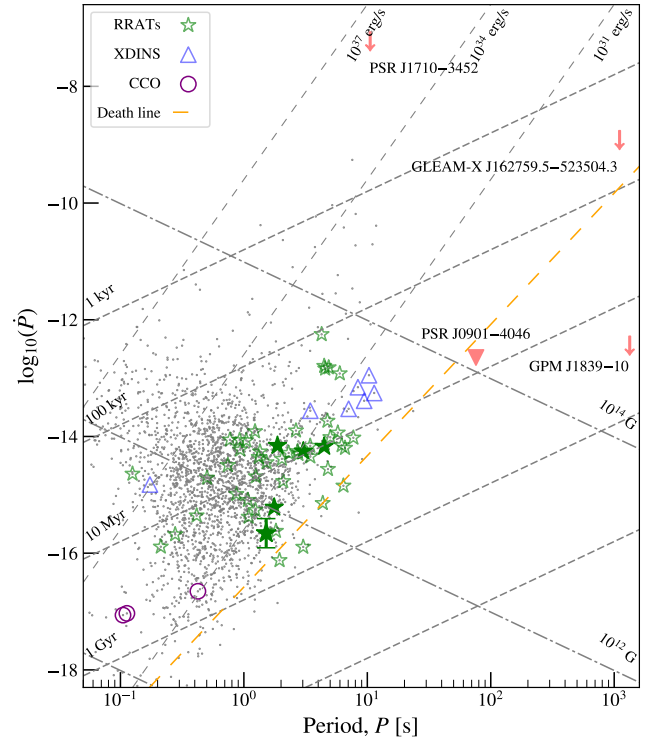


Figure 11. P - \dot{P} diagram showing the five RRATs with timing solutions reported in this paper as filled in stars. All other RRATs are unfilled stars. The death line is that of Equation (4) in Zhang et al. (2000). The long period sources that could be NSs; GLEAM-X J162759.5–523504.3 (Hurley-Walker et al. 2022b) and GPM J1839–10 (Hurley-Walker et al. 2023), or are definitively NSs; PSR J0901–4046 (Caleb et al. 2022a)) are shown in red where a down arrow signifies the value is an upper limit on \dot{P} . The NS classes of thermal X-ray isolated emitters (XDINS) and the central compact objects (CCOs) are also shown.

The discovery of the 17.5-second source MTP0044 further demonstrates the important role of single pulse searches. In this period regime, conventional periodicity searches would only integrate over ~ 50 rotations, thus failing to obtain a signal of sufficient S/N, especially for sources as intermittent as MTP0044. We choose to refrain from labelling MTP0044 as an RRAT as no periodicity searches of the discovery observation data was possible. MTP0044 cannot yet be placed in P - \dot{P} space, but is similar in spin period to sources beyond the pulsar death line, for which explanations of their coherent radio emission have been difficult to pin down. The 421-second transient discovered by CHIME (Dong et al. 2024) highlights the success of single pulse searches in the period range $10 < P < 1000$ s. Above this period range, the on-pulse region becomes too wide for pulsar-like duty cycles. Despite this, these searches may yet be sensitive to microstructure within pulses of even slower NSs, such as the LPTs identified by image-domain searches with the SKA precursors ASKAP (VAST; Murphy et al. 2021) and the MWA (GLEAM-X; Hurley-Walker et al. 2022a).

MeerTRAP sources show some exceptionality compared to the bulk of the known RRAT population. A histogram of DMs of all Galactic transients from MeerTRAP compared to the rest of the RRAT population is shown in Figure 10. The general trend suggested by Bezuidenhout et al. (2022) that MeerTRAP is sampling a population of larger DMs remains true. The MeerTRAP sources have a median value of 130 pc cm^{-3} , higher than that of 100 pc cm^{-3} for known

RRATs. Further to this, both MTP0018 and MTP0044 exceed the Galactic DM contribution predicted by the ymw16 model. Unless the Galactic electron density is being underestimated along these lines of sight, MeerTRAP could be sensitive to a sample of Galactic halo transients. Curiously, despite DM values exceeding 400 pc cm^{-3} , we were not able to measure a scattering timescale for any of the brightest pulses from these sources.

The five sources for which we have found timing solutions are shown on the $P-\dot{P}$ plot in Figure 11. The distribution of these sources and the known RRAT population when compared with the characteristic age, magnetic field strength and spin-down luminosity contours suggests that MeerTRAP is sampling RRATs with a lower spin-down luminosity, but not any particular extremity in magnetic field strength or age. It is not clear on this plot what the distribution in P of each population is, so we show same comparison as before but for spin period in the lower plot of Figure 10. The distributions tentatively show that MeerTRAP may be sampling the more slowly rotating NS population, as the median of the MeerTRAP sources is 2.4 s compared to the value of 1.5 s for the known RRATs.

4.2 RRAT timing and pulse widths

Our method for measuring TOAs produced accurate and precise arrival times. Once a spin period accurate to a few hundred microseconds was found, we found that sources with many detections such as MTP0014 and MTP0020 did not require a position more accurate than that provided by a CB detection to phase connect pulses several weeks apart. This is despite pronounced pulse jitter of ~ 30 ms due to pulse-to-pulse profile variation or the variable compatibility of the Gaussian with the pulse shapes. However, localisations of near arcsecond precision provided by SEEKAT or imaging were essential for phase-connecting the TOAs of sources with fewer and less frequent detections, e.g. MTP0023 and MTP0034. We did not use our timing solutions to make integrated pulse profiles of the five timed RRATs. Instead, we propose that the histogram of residuals in Figure 3 can potentially serve as a proxy for this. An obvious exception is MTP0023; the residual distribution of MTP0023 is unimodal, thus does not reflect the presence of multiple components that we repeatedly observe. We suspect that, unlike for the other four timed RRATs, the overlap between components is too great to allow the TOAs measured in this way to align into residual bands. To check how robust the other residual distributions are at showing the average pulse profile, we calculated the widths of the pulses for these five RRATs. We also do this for three other new RRATs with a sufficiently large population of pulses: MTP0031, MTP0039 and MTP0045.

To measure the pulse width, specifically the width at 50 per cent of the peak flux, w_{50} , we use the `fitvonMises` function in the pulsar data analysis package `PSRSALSA`²⁵ (Weltevrede 2016). The data are reduced using tools from the pulsar data analysis package `PSRCHIVE`²⁶ (Hotan et al. 2004; van Straten & Bailes 2011). We start by using `PSRCHIVE/paas` to make a noise-free template of the brightest pulse from the source at each frequency band it has been detected at. Then, for each pulse, we produce its dedispersed time series by using `PSRCHIVE/DSPSR` and `PSRCHIVE/pam` to convert and downsample the data. Then, we interactively select the off-pulse region before fitting the template to the pulse with the `PSRSALSA/fitvonMises`

function, which fits the pulse shape by refining the concentration parameter of the von-Mises distribution. The model has noise added to it using the noise statistics of the off-pulse region we had selected. Finally, we find w_{50} and its uncertainty with `fitvonMises`, bootstrapped with 100 iterative fits of the model to the pulse. For each pulse, we make 10 such measurements of w_{50} and calculate the mean weighted by their uncertainties to obtain our final value for w_{50} . Pulses for which the data are too badly affected by RFI or where the pulse is too faint for the template to be fitted are rejected.

We found that fitting $>N$ von-Mises functions to a pulse profile with N components became problematic as the spare fit component(s) would find power within noise features and disrupt the fit. As a result, we are mostly measuring widths of individual components, rather than the average profile. For sources which have only shown single component pulses like MTP0017, MTP0034, MTP0039 and MTP0045, we assumed that the average pulse profile is dominated by, or entirely consists of, a single component. The residual distributions for MTP0017 and MTP0034 suggests this is true for these sources and supports this assumption. We also base the assumption on having not actually seen a multicomponent pulse profile from these four RRATs. For MTP0014, we inspected all the detections by eye and found that approximately 10 per cent have a two components, thus fitting a single component template is appropriate for the majority of pulses. Similarly for MTP0020, we know from its timing residuals and component switching that it is rare for more than one component to be present. MTP0023 and MTP0031 have decidedly more complicated pulse-to-pulse variation and a two-component template was required for one of the frequency bands. For MTP0023, a majority of UHF pulses had two components, similar in form to the discovery pulse in Figure 2, whereas the L-band pulses were mainly singly-peaked. This is probably due to the increased sensitivity of the UHF targeted observations, not due to frequency-dependent profile changes. A significant proportion of pulses from MTP0031 show the main pulse and precursor, so a two-component template was used. The w_{50} distributions and the shape of the templates used are shown in Figure 12. The templates are not intended to show frequency evolution of the pulse shape, instead they only show the noise-free model of the brightest pulse of that frequency. The width distribution for MTP0014 at L-band is the most populous and appears to agree with the residual distributions of Figure 3. We see two distinct peaks; a small range of narrow pulses followed by a broad range of wider pulses. This is to be expected given the relative share of TOAs we detect from each component, and suggests that the leading component is wider than the trailing component(s). The same is seen for MTP0020, though the reverse is true for widths; the trailing component dominates and is the wider of the two. Interestingly, the widths of MTP0017 are bimodal, peaking at approximately 13 ms and 22 ms. This is not predicted by the residuals, as their distribution is not clearly bimodal, and there is no preference for smaller error TOAs in residual space. This could mean that there are indeed two components are never concurrent or are closely overlapping such that they are resolved out by the pulse jitter.

In most of the pulses between MTP0023 and MTP0031, the combined width of two components was not measured as the precursor did not contain enough power. Four pulses from MTP0031 had precursors strong enough to be included in the width measurement, for which we found widths between 103 ± 6 ms and 124 ± 1 ms. These correspond to a duty cycle of between 4-5 per cent. These width distributions have allowed a better understanding of the residual distributions in Figure 3 and how they are affected by the pulse-to-pulse variability unique to each RRAT. We note that the ability to measure

²⁵ <https://github.com/weltevrede/psrsalsa> by Patrick Weltevrede

²⁶ <https://psrchive.sourceforge.net/index.shtml>

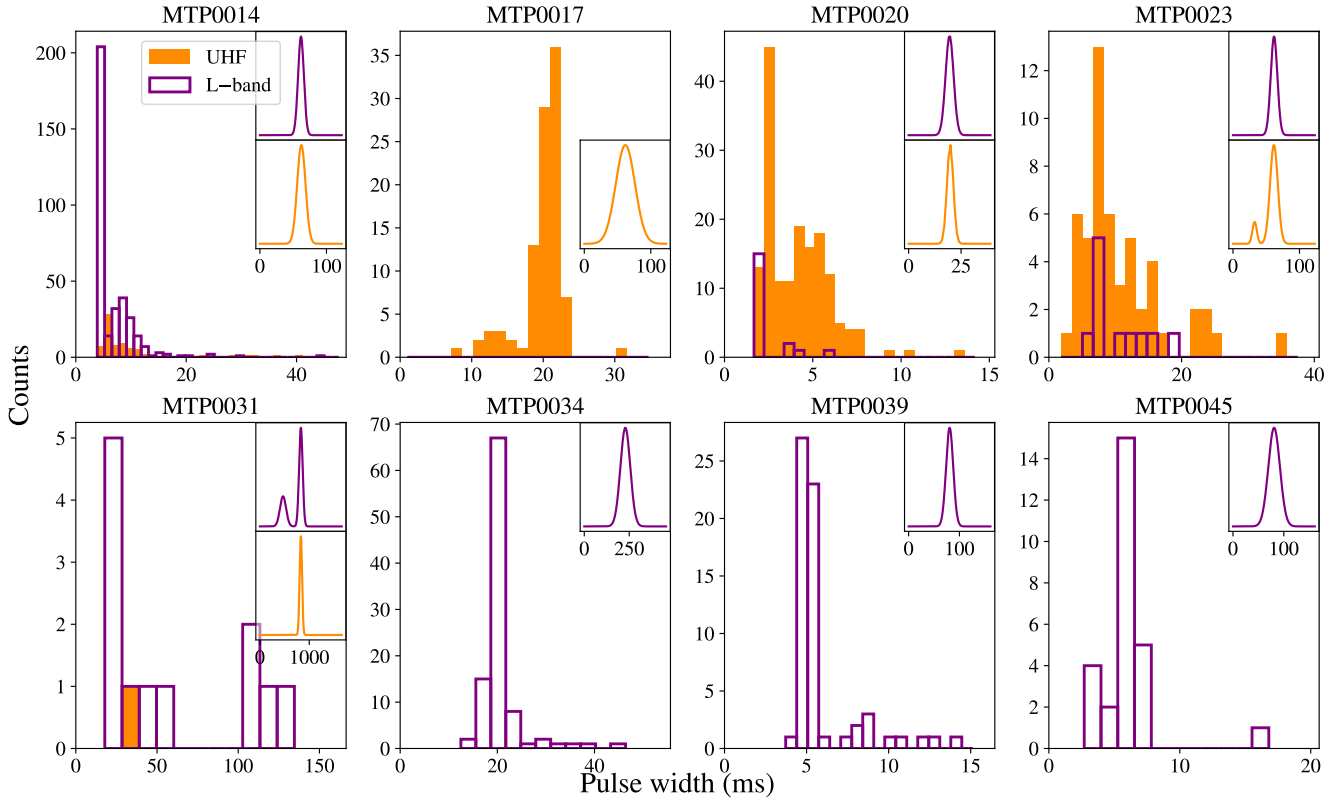


Figure 12. Histograms of w_{50} in milliseconds for eight of the new RRATs. The templates for the respective band they have been fitted to are shown on the right flank of each panel, also in units of milliseconds. The widths have not been scaled to a common frequency.

widths of only a few milliseconds demonstrates the importance of retaining sub-millisecond sampling times for single pulse data.

5 CONCLUSIONS

We have presented the latest 26 Galactic transients to be discovered by MeerTRAP, following the 14 that have already been published (Bezuidenhout et al. 2022; Caleb et al. 2022a; Surin et al. 2023). The majority are identified as members of the RRAT class of neutron stars. We also presented detections of three sources independently discovered elsewhere, including two pulsars that were detected whilst piggy-backing on the MMGPS–L observations that were later identified in periodicity searches. We calculated arrival times and found phase-connected timing solutions for five RRATs and estimate spin periods for an additional eight. For MTP0044/PSR J2218+2902, we found a spin period of 17.5 s, adding to a growing population of slowly rotating neutron stars that challenge magnetospheric radio emission models. This continues the trend of single pulse searches uncovering longer period transients. The complex structure, brightness and variability of pulses from MTP0021/PSR J0219–06 and MTP0023/PSR J1319–4536 recommend them for further study. MeerTRAP is sampling a population of higher DM, longer period Galactic transients. The DMs of MTP0018 and MTP0044/PSR J2218+2902 infer their locations could be in the Galactic halo depending on the predicted electron density along their line of sight. The large fraction of sources to have been seen only further hints at existence of a significant population of these sources within the Milky Way Galaxy. The importance of commensal single

pulse searches operating as close to full-time as possible continues to be demonstrated.

ACKNOWLEDGEMENTS

The MeerKAT telescope is operated by the South African Radio Astronomy Observatory (SARAO), which is a facility of the National Research Foundation, itself an agency of the Department of Science and Innovation. All the authors thank the MeerKAT LSP teams for allowing commensal observing and the staff at SARAO for scheduling MeerKAT observations. MeerTRAP observations use the FB-FUSE and TUSE computing clusters for data acquisition and storage. These instruments were designed, funded and installed by the Max-Planck Institut für Radioastronomie (MPIfR) and the Max-Planck-Gesellschaft. This project has received funding from the European Research Council (ERC) under the European Union’s Horizon 2020 research and innovation programme (grant agreement no. 694745). JDT acknowledges funding from the United Kingdom’s Research and Innovation Science and Technology Facilities Council (STFC) Doctoral Training Partnership, project code 2659479. M.C. acknowledges support of an Australian Research Council Discovery Early Career Research Award (project number DE220100819) funded by the Australian Government. IPM further acknowledges funding from an NWO Rubicon Fellowship, project number 019.221EN.019. For the purpose of open access, the author has applied a Creative Commons Attribution (CC BY) licence to any Author Accepted Manuscript version arising. J.D.T. thanks Dr. O. G. Dodge for his help with scripting. The authors would like to thank the reviewer for their helpful comments and recommendations that improved this publication.

This research used version 2.2.0 of the ATNF Pulsar Catalogue. This research has made use of the SIMBAD data base, operated at CDS, Strasbourg, France (Wenger et al. 2000). This research has made use of NASA's Astrophysics Data System Bibliographic Services.

DATA AVAILABILITY

The data underlying this article are available in Zenodo, at [10.5281/zenodo.14646142](https://doi.org/10.5281/zenodo.14646142). Other data will be made available to those with a reasonable request to the authors.

REFERENCES

- Bailes M., et al., 2016, in MeerKAT Science: On the Pathway to the SKA. p. 11 ([arXiv:1803.07424](https://arxiv.org/abs/1803.07424)), [doi:10.22323/1.277.0011](https://doi.org/10.22323/1.277.0011)
- Barr E. D., 2018, in Weltevrede P., Perera B. B. P., Preston L. L., Sanidas S., eds, Vol. 337, Pulsar Astrophysics the Next Fifty Years. pp 175–178, [doi:10.1017/S1743921317009036](https://doi.org/10.1017/S1743921317009036)
- Bause M. L., Herrmann W., Spitler L. G., 2024, *A&A*, **686**, A144
- Beniamini P., Wadiasingh Z., Hare J., Rajwade K. M., Younes G., van der Horst A. J., 2023, *MNRAS*, **520**, 1872
- Bezuidenhout M. C., et al., 2022, *MNRAS*, **512**
- Bezuidenhout M. C., et al., 2023, *RAS Techniques and Instruments*, **2**, 114
- Bhattacharyya B., et al., 2018, *MNRAS*, **477**, 4090
- Burke-Spolaor S., Bailes M., 2010, *MNRAS*, **402**, 855
- Burke-Spolaor S., et al., 2011, *MNRAS*, **416**, 2465
- CHIME/FRB Collaboration et al., 2018, *ApJ*, **863**, 48
- Caleb M., et al., 2022a, *Nature Astronomy*, **6**, 1
- Caleb M., et al., 2022b, *MNRAS*, **510**, 1996
- Caleb M., et al., 2024, *Nature Astronomy*, **8**, 180
- Camilo F., et al., 2018, *ApJ*, **856**, 180
- Chen W., Barr E., Karuppusamy R., Kramer M., Stappers B., 2021, *Journal of Astronomical Instrumentation*, **10**, 2150013
- Cordes J. M., Chatterjee S., 2019, *ARA&A*, **57**, 417
- Cordes J. M., Lazio T. J. W., 2002, *arXiv e-prints*, pp astro-ph/0207156
- Cordes J. M., McLaughlin M. A., 2003, *ApJ*, **596**, 1142
- Cordes J. M., Rickett B. J., 1998, *ApJ*, **507**, 846
- Deneva J. S., et al., 2016, *ApJ*, **821**, 10
- Deneva J. S., McLaughlin M., Olszanski T. E. E., Lewis E. F., Pang D., Freire P. C. C., Bagchi M., Stovall K., 2024, *ApJS*, **271**, 23
- Dong F. A., et al., 2023, *MNRAS*, **524**, 5132
- Dong F. A., et al., 2024, *arXiv e-prints*, p. [arXiv:2407.07480](https://arxiv.org/abs/2407.07480)
- Driessen L. N., et al., 2022, *MNRAS*, **512**, 5037
- Driessen L. N., et al., 2024, *MNRAS*, **527**, 3659
- Duchesne S. W., et al., 2024, *Publ. Astron. Soc. Australia*, **41**, e003
- Eatough R. P., Keane E. F., Lyne A. G., 2009, *Monthly Notices of the Royal Astronomical Society*, **395**, 410
- Fender R., et al., 2016, in MeerKAT Science: On the Pathway to the SKA. p. 13 ([arXiv:1711.04132](https://arxiv.org/abs/1711.04132)), [doi:10.22323/1.277.0013](https://doi.org/10.22323/1.277.0013)
- Fiore W., et al., 2023, *ApJ*, **956**, 40
- Gupta N., et al., 2016, in MeerKAT Science: On the Pathway to the SKA. p. 14 ([arXiv:1708.07371](https://arxiv.org/abs/1708.07371)), [doi:10.22323/1.277.0014](https://doi.org/10.22323/1.277.0014)
- Hale C. L., et al., 2021, *Publ. Astron. Soc. Australia*, **38**, e058
- Hessels J. W. T., et al., 2019, *ApJ*, **876**, L23
- Hobbs G. B., Edwards R. T., Manchester R. N., 2006, TEMPO2, a new pulsar-timing package - I. An overview, [doi:10.1111/j.1365-2966.2006.10302.x](https://doi.org/10.1111/j.1365-2966.2006.10302.x)
- Hobbs G., Lyne A. G., Kramer M., 2010, *MNRAS*, **402**, 1027
- Hosenie Z., 2021, PhD thesis, The University of Manchester, <https://research.manchester.ac.uk/en/studentTheses/feature-detection-and-classification-in-streaming-and-non-streaming-pulsars>
- Hotan A. W., van Straten W., Manchester R. N., 2004, *Publ. Astron. Soc. Australia*, **21**, 302
- Hurley-Walker N., et al., 2022a, *Publ. Astron. Soc. Australia*, **39**, e035
- Hurley-Walker N., et al., 2022b, *Nature*, **601**, 526
- Hurley-Walker N., et al., 2023, *Nature*, **619**, 487
- Jankowski F., 2022, Scatfit: Scattering fits of time domain radio signals (Fast Radio Bursts or pulsars), Astrophysics Source Code Library, record ascl:2208.003
- Jankowski F., van Straten W., Keane E. F., Bailes M., Barr E. D., Johnston S., Kerr M., 2018, *MNRAS*, **473**, 4436
- Jankowski F., et al., 2022, in Ruiz J. E., Pierfedereci F., Teuben P., eds, Astronomical Society of the Pacific Conference Series Vol. 532, Astronomical Society of the Pacific Conference Series. p. 273 ([arXiv:2012.05173](https://arxiv.org/abs/2012.05173)), [doi:10.48550/arXiv.2012.05173](https://doi.org/10.48550/arXiv.2012.05173)
- Jankowski F., et al., 2023, *MNRAS*, **524**, 4275
- Jonas J., 2018, in Proceedings of MeerKAT Science: On the Pathway to the SKA. Proceedings of Science, p. 1, [doi:10.22323/1.277.0001](https://doi.org/10.22323/1.277.0001)
- Karako-Argaman C., et al., 2015, *ApJ*, **809**, 67
- Karuppusamy R., Stappers B. W., van Straten W., 2010, *A&A*, **515**, A36
- Keane E. F., Kramer M., 2008, *MNRAS*, **391**, 2009
- Keane E. F., McLaughlin M. A., 2011, *Bulletin of the Astronomical Society of India*, **39**, 333
- Keane E. F., Ludovici D. A., Eatough R. P., Kramer M., Lyne A. G., McLaughlin M. A., Stappers B. W., 2010, *MNRAS*, **401**, 1057
- Keane E. F., et al., 2018, *MNRAS*, **473**, 116
- Kramer M., et al., 2021, *MNRAS*, **504**, 2094
- Kramer M., Liu K., Desvignes G., Karuppusamy R., Stappers B. W., 2024, *Nature Astronomy*, **8**, 230
- Kumar A., Maan Y., Bhusare Y., 2024, *arXiv e-prints*, p. [arXiv:2406.12804](https://arxiv.org/abs/2406.12804)
- Lanman A. E., et al., 2022, *ApJ*, **927**, 59
- Lehmensiek R., Theron I. P., 2012, in Proceedings of the 2012 International Conference on Electromagnetics in Advanced Applications, ICEAA'12. pp 321–324, [doi:10.1109/ICEAA.2012.6328642](https://doi.org/10.1109/ICEAA.2012.6328642)
- Lehmensiek R., Theron I. P., 2014, in The 8th European Conference on Antennas and Propagation (EuCAP 2014). pp 880–884, [doi:10.1109/EuCAP.2014.6901903](https://doi.org/10.1109/EuCAP.2014.6901903)
- Lewandowski W., Kowalińska M., Kijak J., 2015, *MNRAS*, **449**, 1570
- Li D., Pan Z., 2016, *Radio Science*, **51**, 1060
- Lyne A. G., McLaughlin M. A., Keane E. F., Kramer M., Espinoza C. M., Stappers B. W., Palliyaguru N. T., Miller J., 2009, *MNRAS*, **400**, 1439
- Malenta M., et al., 2020, in Pizzo R., Deul E. R., Mol J. D., de Plaa J., Verkouter H., eds, Astronomical Society of the Pacific Conference Series Vol. 527, Astronomical Data Analysis Software and Systems XXIX. p. 457
- Manchester R. N., Hobbs G. B., Teoh A., Hobbs M., 2005, *AJ*, **129**, 1993
- McLaughlin M. A., et al., 2006, *Nature*, **439**, 817
- McMullin J. P., Waters B., Schiebel D., Young W., Golap K., 2007, in Shaw R. A., Hill F., Bell D. J., eds, Astronomical Society of the Pacific Conference Series Vol. 376, Astronomical Data Analysis Software and Systems XVI. p. 127
- Men Y. P., et al., 2019, *MNRAS*, **488**, 3957
- Michilli D., et al., 2018, *MNRAS*, **480**, 3457
- Morello V., Rajwade K. M., Stappers B. W., 2022, *MNRAS*, **510**, 1393
- Morello V., Rajwade K. M., Stappers B. W., 2023, IQRM: IQRM interference flagging algorithm for radio pulsar and transient searches, Astrophysics Source Code Library, record ascl:2311.008
- Murphy T., et al., 2021, *Publ. Astron. Soc. Australia*, **38**, e054
- Ng C., et al., 2015, *MNRAS*, **450**, 2922
- Norris R. P., et al., 2021, *Publ. Astron. Soc. Australia*, **38**, e046
- Offringa A. R., et al., 2014, *MNRAS*, **444**, 606
- Oppermann N., Yu H.-R., Pen U.-L., 2018, *MNRAS*, **475**, 5109
- Padmanabh P. V., et al., 2023, *MNRAS*, **524**, 1291
- Patel C., et al., 2018, *ApJ*, **869**, 181
- Petroff E., Hessels J. W. T., Lorimer D. R., 2022, *A&ARv*, **30**, 2
- Price D. C., Flynn C., Deller A., 2021, *Publ. Astron. Soc. Australia*, **38**, e038
- Rajwade K., et al., 2021, in 43rd COSPAR Scientific Assembly. Held 28 January - 4 February. p. 1194
- Rajwade K. M., et al., 2022, *MNRAS*, **514**, 1961
- Rajwade K. M., et al., 2024, *MNRAS*, **530**, 1000
- Rykoff E. S., et al., 2014, *ApJ*, **785**, 104
- Sand K. R., et al., 2024, *arXiv e-prints*, p. [arXiv:2408.13215](https://arxiv.org/abs/2408.13215)
- Sanidas S., Caleb M., Driessen L., Morello V., Rajwade K., Stappers B. W., 2018, in Weltevrede P., Perera B. B. P., Preston L. L., Sanidas S., eds,

- IAU Symposium Vol. 337, Pulsar Astrophysics the Next Fifty Years. pp 406–407, doi:[10.1017/S1743921317009310](https://doi.org/10.1017/S1743921317009310)
- Scholz P., et al., 2016, *ApJ*, **833**, 177
- Seymour A., Michilli D., Pleunis Z., 2019, DM_phase: Algorithm for correcting dispersion of radio signals, Astrophysics Source Code Library, record ascl:1910.004
- Shapiro-Albert B. J., McLaughlin M. A., Keane E. F., 2018, *ApJ*, 866
- Stappers B. W., Kramer M., 2016, in Proceedings of Science. p. 9, doi:[10.22323/1.277.0009](https://doi.org/10.22323/1.277.0009)
- Surnis M. P., et al., 2023, *MNRAS*, **526**, L143
- Swiggum J. K., et al., 2015, *ApJ*, **805**, 156
- Tan C. M., et al., 2018, *ApJ*, **866**, 54
- Taylor A. R., Jarvis M., 2017, in Materials Science and Engineering Conference Series. IOP, p. 012014, doi:[10.1088/1757-899X/198/1/012014](https://doi.org/10.1088/1757-899X/198/1/012014)
- Tian J., et al., 2024, *MNRAS*,
- Tyul'bashev S. A., et al., 2018, *Astronomy Reports*, **62**, 63
- Wang Z., et al., 2024, *arXiv e-prints*, p. [arXiv:2409.10316](https://arxiv.org/abs/2409.10316)
- Weltevrede P., 2016, *A&A*, **590**, A109
- Wenger M., et al., 2000, *A&AS*, **143**, 9
- Yamasaki S., Totani T., 2020, *ApJ*, **888**, 105
- Yao J. M., Manchester R. N., Wang N., 2016, *ApJ*, **835**, 29
- Zhang B., Harding A. K., Muslimov A. G., 2000, *ApJ*, **531**, L135
- Zhou D. J., et al., 2023, *Research in Astronomy and Astrophysics*, **23**, 104001
- van Straten W., Bailes M., 2011, *Publ. Astron. Soc. Australia*, **28**, 1

APPENDIX A: IMAGES AND DM FIT STATISTICS

This paper has been typeset from a $\text{\TeX}/\text{\LaTeX}$ file prepared by the author.

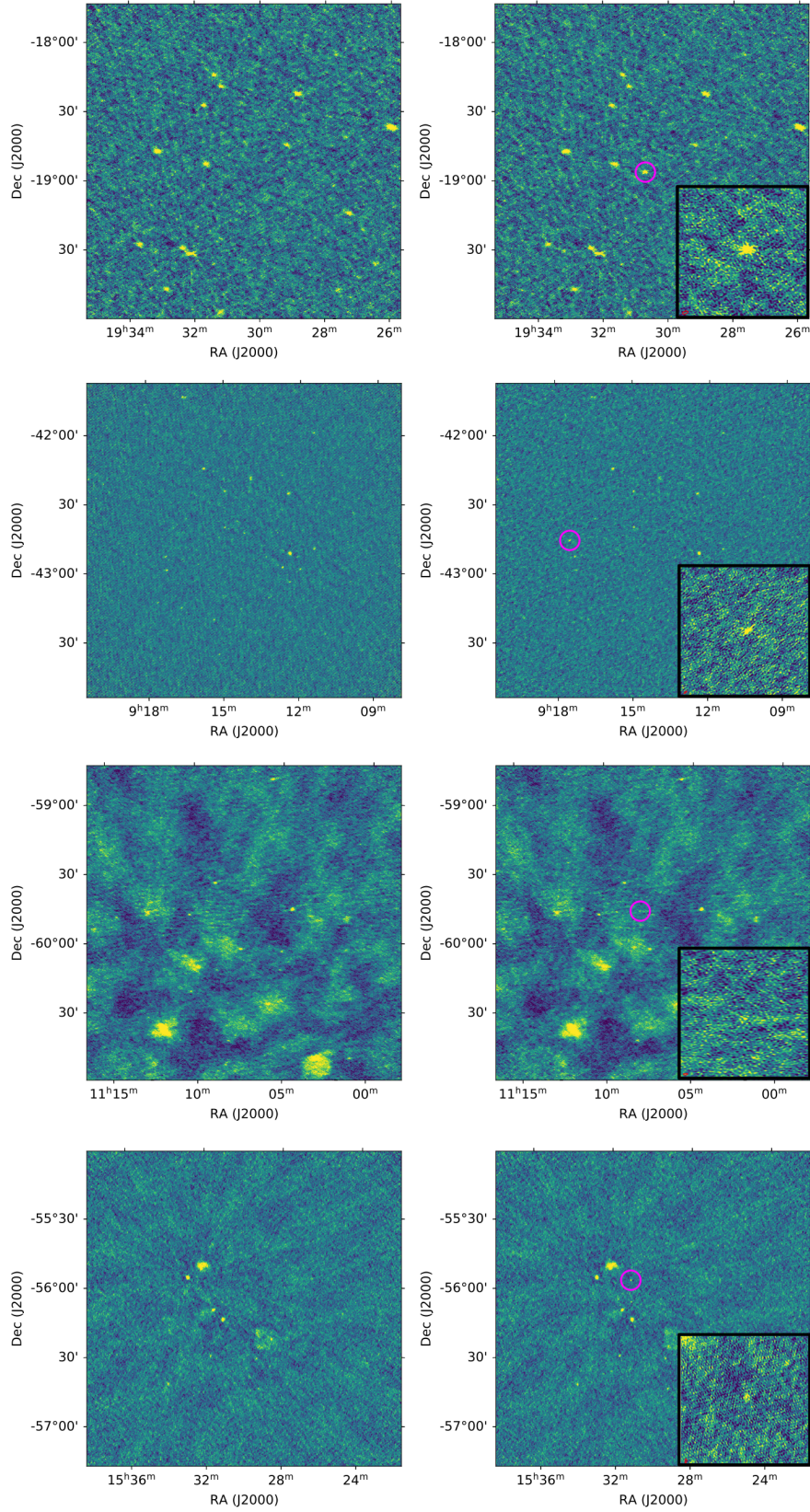


Figure A1. From top down: Images of the positions of MTP0020, MTP0031, MTP0034 and MTP0045, integrated over the duration of the pulse (right) and before the pulse detection (left). The magenta circle marks the transient source identified at the time of the pulse detection. The inset at the bottom right corner of the on-source image is a zoomed in view centred on the source. The red ellipse at the bottom left corner of the inset indicates the synthesised beam.

Table A1. Fit statistics from SCATFIT for the sources we fit. The S/N is for the pulse dedispersed at the tabulated DM, and determined by SPYDEN.

Source	DM (pc cm ⁻³)	Uncertainty	S/N	Pulse epoch		Reduced- χ^2	BIC
MTP0014	71.299	0.031	53.8	2023 May 08	UTC 23:32:16	1.3	4.1
MTP0016	41.162	0.349	21.6	2020 Dec 25	UTC 01:59:07	1.2	2.8
MTP0017	31.517	0.210	18.8	2022 Jun 17	UTC 08:42:19	1.2	2.9
MTP0018	38.837	0.307	9.7	2021 May 10	UTC 16:11:46	1.7	2.0
MTP0020	63.143	0.009	74.9	2021 Jun 22	UTC 03:41:45	2.1	7.9
MTP0024	41.007	0.501	13.3	2021 Jun 07	UTC 01:46:13	0.5	-3.3
MTP0026	206.828	0.253	10.0	2021 Jun 25	UTC 23:05:53	0.5	-3.0
MTP0028	440.298	0.239	23.1	2021 Aug 10	UTC 20:33:27	0.8	-0.4
MTP0029	201.422	0.222	17.3	2021 Aug 20	UTC 21:46:32	0.6	-2.1
MTP0032	271.516	0.454	11.0	2021 Oct 12	UTC 15:32:17	1.7	0.6
MTP0034	92.736	0.447	27.8	2023 Feb 26	UTC 04:38:30	0.9	0.6
MTP0035	224.463	0.220	11.1	2021 Oct 26	UTC 13:02:04	2.8	4.0
MTP0036	128.894	0.716	9.4	2021 Oct 30	UTC 01:20:14	0.4	-3.8
MTP0038	126.711	0.389	16.1	2021 Dec 09	UTC 06:12:23	4.0	11.2
MTP0039	95.313	0.091	36.5	2021 Dec 20	UTC 10:40:29	0.2	-11.6
MTP0040	264.142	1.091	9.4	2021 Dec 16	UTC 09:20:27	2.0	1.0
MTP0042	250.353	0.656	12.9	2021 Oct 08	UTC 18:56:32	0.5	-2.4
MTP0044	55.795	0.389	16.5	2022 Jan 02	UTC 13:04:19	1.3	3.3
MTP0045	56.602	0.563	13.8	2021 Dec 20	UTC 03:55:39	1.8	5.6
MTP0046	254.170	1.497	8.8	2022 Jan 15	UTC 10:20:15	2.0	1.0
MTP0047	152.396	0.357	10.7	2022 Feb 19	UTC 10:13:36	2.0	0.1
MTP0048	151.559	0.457	9.4	2022 Feb 03	UTC 06:01:15	0.9	0.4
MTP0049	346.506	0.678	9.8	2022 Feb 06	UTC 06:06:28	0.9	-1.3